A Statistical Overview of the Spatial Atmospheric Variability Over Isfjorden, Svalbard

En statistisk översikt av atmosfärens rumsliga variabilitet över Isfjorden, Svalbard

Agnes Stenlund

A Statistical Overview of the Spatial Atmospheric Variability Over Isfjorden, Svalbard

AGNES STENLUND

November 9, 2022

Supervisor:
Assoc. Prof. Marius O. Jonassen
The University Center in Svalbard
Department for Geophysics

UNIS
The University Centre in Svalbard

UPPSALA
UNIVERSITET

Abstract

The atmospheric spatial variability over Isfjorden, Svalbard, was investigated through statistical data analysis. The data used in the thesis was measured by mobile weather stations installed on three ships crossing the fjord, and two stationary weather stations close to the shoreline, during the autumn of 2021 and spring to autumn 2022. The spatial distributions of temperature, specific humidity, and wind speed were filtered into categories of season, ambient wind direction, and ambient wind speed, before they were studied.

Gradients in temperature and humidity are re-occurring patterns along the Isfjorden axis during various seasons and wind directions. The temperature gradient was found to be partly generated by local drainage winds and further to be connected to the difference between air and sea surface temperature. The humidity gradient was consistent across all seasons and predominantly controlled by advection and differences in available water from surrounding land surfaces. A peak in wind speed around the mouth of Sassenfjorden indicated forced channeling effects, as the pattern dominated when the ambient wind aligned with the axis of the fjord. The results indicate local processes that can be expected from previous research.

Swedish Summary

Atmosfärens rumsliga variation över Isfjorden, Svalbard, undersöktes i denna studie genom statistisk dataanalys. Datan mättes av mobila väderstationer installerade på tre båtar som korsade fjorden på daglig basis, tillsammans med två stationära stationer placerade i närheten av fjordens strandkant. Mätningar pågick under hösten 2021 samt vår till höst 2022.

De rumsliga distributionerna av temperatur, absolut fuktighet och vindhastighet filtrerades in i kategorier baserade på årstid, omgivande vindriktning och omgivande vindhastighet, innan de studerades. Signalerna som förekom i datan varierade mellan de meteorologiska storheterna, men indikerade lokala processer som var förväntade baserat på tidigare forskning. I datan presenterades återkommande mönster av gradienter i temperatur och fuktighet längs Isfjordens axel, för flera årstider och vindriktningar. Temperaturgradienten tros delvis genereras av lokala fallvindar och ett samband fastställdes mellan gradientriktningen och relationen mellan atmosfärens och havsytans temperatur. Fuktighetsgradienten var konsekvent förekommande under hela mätperioden och visades främst begränsas av olika närliggande ytors tillgång till vatten. Särskilt höga vindhastigheter runt Sassenfjordens öppning indikerade kanaliseringseffekter drivna av den geostrofiska vinden. Signalen förekom primärt då den omgivande vindriktningen sammanföll med fjordens riktning.

Acknowledgement

I would like to thank Assoc. Prof. Erik Sahlée at Uppsala University and Assoc. Prof. Marius O. Jonassen at the University Center in Svalbard (UNIS) for their commitment, making this thesis possible, and for supporting me throughout this project. I also, naturally, want to acknowledge the work of PhD candidate Lukas Frank at UNIS, who has been an incredibly encouraging, dedicated, and supporting guide and friend from the beginning to the very end. Thanks also to former captain of the superhero troop, nowadays PhD candidate at the University of Graz, Florina Schalamon who has helped and always offered to do whatever she could to make my life easier.

I also would like to thank the companies Polarcharter, Brim Explorer and Hurtigruten, that have been open and excited about promoting science and kindly let us set up instrumentation at their ships. The help from people at UNIS regarding technicalities and logistics around IWIN have been very valuable and appreciated.

And, on the most personal level as this project marks the end of many years of studies, thanks to:

Several constellations of people in Svalbard, for including me in so many ways. The entire AGF-350/850 class of spring 2022 for being my first Svalbard family, my * gang for the adventures and Sunday morning debrief sessions, my office mates for sharing their energy and wisdom – especially Charlotte for keeping me alive with incredible kindness and humour. Thanks to everyone that I have shared a pizza or a dance with. Like the northern lights and Arctic nature were not enough on their own.

To all of my friends in Uppsala, who have carried me through early mornings and late nights during shifting seasons over multiple years. Who have endlessly discussed everything from triple integrals, signal analysis, and soil chemistry to music, politics, and dreams. Thanks for constantly reminding me that I always think that the current course is the worst and hardest one I have ever taken. You have been the light of my study life and without you I would have dropped out at basic mechanics.

Lastly, thanks to Mattias and to my family for never really caring about me doing anything except being me. Apparently, that is a good way of inspiring someone to become an engineer.

Agnes Stenlund
Uppsala, 2022

Populärvetenskaplig sammanfattning

Lösningar till globala miljöförändringar är en av vår tids mest aktuella, omdiskuterade och efterfrågade vetenskapliga utmaningar. Allra mest framträdande är förändringarna i de arktiska regionerna, där ökningen av medeltemperatur nära markytan har visats vara flera grader högre än för övriga delar av världen. Vidare förekommer stora problem angående väderprognostisering på höga latituder, delvis eftersom atmosfäriska processer lokalt kan skilja sig från tendenser på större skala, som ett resultat av komplex terräng och den begränsande perioden av inkommande kortvågig strålning från solen. Bristen på kvalitativa väderprognoser kan riskera säkerheten för invånarna i regionen, inte minst med tanke på att extrema väder återkommande förekommer, och påverkar även verksamheter som båttrafik och turism i området. Denna särskilt utsatta position påtalar ett behov av klimatforskning i regionen, samt utveckling av pålitliga vädermodeller att möta framtida förändringar med.

Detta arbete bidrog med ny information angående den rumsliga atmosfäriska variationen (i temperatur, fuktighet och vindhastighet) över Isfjorden, den största fjorden på ön Spitsbergen i Svalbards skärgård. I en av Isfjordens grenar ligger Longyearbyen, huvudbosättning för regionen, och Isfjorden utgör i tillägg den huvudsakliga transportsträckan för båttrafik mellan Svalbard och fastlandet. Fjordens väderförhållanden är därav viktiga både för boende och för besökande turister.

För att samla in data till projektet installerades mobila, automatiska väderstationer på tre stycken turistbåtar som korsade Isfjorden på daglig basis. För att samla in referensvärden över fjordens allmänna, atmosfäriska tillstånd installerades även en stationär väderstation på en udde som sträcker sig ut i Isfjorden från dess nordvästra kust. Störningar i referensdatan vid särskilda vindriktningar krävde användning av ytterligare en stationär väderstation, då korrektion av värdena visade sig vara nödvändigt. Mätningar pågick från mars till oktober 2022, och även data från augusti till oktober 2021 användes.

Genom att subtrahera referensvärdena från de mobila mätningarna i varje tidssteg kunde variationen (avvikelsen från referensvärdet) i temperatur, fuktighet och vindhastighet studeras över Isfjordens olika delar. Datan sorterades i olika kategorier beroende på vilken årstid och storskalig vindriktning eller vindhastighet som rådde under mätningarna. Vidare genomfördes en analys över hur fjordens distribution i meteorologiska variables förändrades över exempelvis årstiderna.

En rad intressanta vädermönster och deras bakomliggande processer identifierades under arbetets gång. Datan visade en återkommande horisontell temperaturskillnad (gradient) på upp till 3.5°C mellan fjordens inre och yttre del under nordliga vindar på våren och hösten. Gradienten förklarades vara ett resultat av advektion av kall luft och fallvindar ned för dalglaciären Nordskiöldbreen i fjordens inre del, i kombination med interaktion mellan Isfjordens interna luft och den västliga, förhållandevis varma marina luften i närheten av fjordens öppning. På sommaren visade sig en speglad tendens, med relativt höga temperaturer i Isfjordens inre del, som resultat av solinstrålningens uppvärmning av land (och vidare ett amplifierat värmeflöde till atmosfären) under polarsommaren. Interaktionen med den marina luften bidrog därav till ett relativt kallt område omkring fjordens öppning istället.

Även en gradient i absolut fuktighet kunde påvisas, med konstant riktning under hela mätperioden och därav oberoende av skiftningar i relationen mellan vatten- och lufttemperatur. Den största horisontella skillnaden mellan den inre och yttre delen av fjorden var 0.6 g/kg under mätperioden. Fuktighetsgradienten konstaterades istället upprätthållas av begränsningen av vattentillgång för evaporation över de landytor som omger fjordens inre delar.

Den rumsliga distributionen av vindhastighet indikerade återkommande kanaliseringseffekter när den geostrofiska vindens riktning sammanföll med riktningen på en av Isfjordens grenfjordar, Sassenfjorden. Vindhastigheten runt Sassenfjordens öppning uppnådde 200% av referenser för västliga vindar och cirka 140% av referenser för östliga vindar.

Contents

List of Abbreviations

- ABL = Astmospheric Boundary Layer

- AWS = Automatic Weather Station

- BHN = Bohemanneset

- BR = Bowen Ratio

- LYR = Longyearbyen

- NWP = Numerical Weather Prediction

- SEB = Surface Energy Balance

1 Introduction

The Svalbard archipelago is located at the periphery of the North-Atlantic storm track, between the northern coast of the Scandinavian mainland and the North Pole, and is hence dominated by frequent changes in air masses and corresponding variability in heat, moisture and wind (Wickström et al. 2020). Along with the awareness about the rapid changes in the near-surface climate of the Svalbard archipelago, even relative to the prevailing global warming, the call for meteorological research in the area has increased (Sotiropoulou et al. 2016, Dahlke et al. 2020, Wickström et al. 2020, IPCC 2021). The strong Arctic warming, known as the Arctic amplification, has been found to be connected to sea ice loss (Dai et al. 2019), meridional circulation patterns (Francis & Vavrus 2012) and complex feedback mechanisms (Stroeve et al. 2012).

The concerning development of the Arctic climate has also brought focus to shortages related to weather prediction in the region. In general, models are performing comparably well for predicting weather on larger scales. The European Centre for Medium-Range Weather Forecasts' (ECMWF's) forecasting accuracy evaluation from 2021 showed high forecasting skills similar to previous years, and in some cases improvements (e.g. regarding precipitation due to updated moist physics in the high-resolution and ensemble forecast, and regarding 2 m temperature, 10 m wind speed and 24 h precipitation for an index aimed at detecting high-impact weather) (Haiden et al. 2021). However, deficiencies in numerical weather prediction models' (NWP) ability to resolve processes smaller than their grid scale (subgrid-scale) are a known issue (Stull 2017). Small and complex processes (such as turbulent mixing, exchange of momentum, heat and matter between the surface and the atmosphere, and radiative transfer) are represented in NWPs through so-called parametrizations. These are methods of simplification replacing the processes that can not be physically represented in the model. Sub-grid processes can be generated by mechanical factors (such as topography) as well as thermodynamic factors (such as local pressure differences) (Kilpeläinen et al. 2011).

The landscape of the Svalbard islands varies dramatically over small spatial scales, and as sufficient parametrization is challenging, the variations in meteorologaical variable due to sub-grid processes are typically not well represented. The network of observations is sparse in the Arctic compared to lower latitudes, which reduces the quality of NWP performance and results in limited available measurement data for research (Nordeng et al. 2007, Køltzow et al. 2019). Additionally, forecasts rarely account for the regional characteristics such as a low tropopause and commonly occurring stability (Nordeng et al. 2007). Consequently, weather forecasts in Svalbard have been found to be less reliable than forecasts at lower latitudes (Nordeng et al. 2007, Kilpeläinen et al. 2011, Jocher et al. 2012, Vihma et al. 2014, Køltzow et al. 2019). The Norwegian Meteorological Institute operates the numerical weather prediction model AROME Arctic, with a horizontal resolution of 2.5 km, to produce weather forecasts for Svalbard and the surrounding seas. Recent evaluation of the model showed large positive temperature errors during cold conditions as well as errors in wind speed estimations (both overestimations and underestimations) (Schalamon 2022). In Isfjorden, the largest fjord on the west coast of Svalbard, local phenomena were also found

not to be represented by the AROME Arctic model. As a consequence of these deficiencies, the region's inhabitants' safety is potentially compromised, considering the risk of extreme weather events in the Arctic (Nordeng et al. 2007, Przybylak et al. 2018). Inaccurate weather prediction can further impact the operations of multiple activities in the region such as ship traffic, resource exploitation and tourism (WMO 2017, Køltzow et al. 2019).

Though the relations between large-scale atmospheric processes and the Arctic climate are fairly well-studied, studies of micro-scale climate are far less common (Vihma et al. 2014). Observations and research on small-scale weather processes are especially sparse for fjord systems and similar deep marine inlets found in mountainous regions (Kilpeläinen & Sjöblom 2010). Focusing on the Forlandsundet region in Svalbard, Przybylak et al. (2018) showed that local spatial patterns of air temperature differs for coastal landscape compared to mountainous and glacial landscape in the Arctic. It was concluded that no general assumption of air temperature and (large-scale) atmospheric circulation relations can be made over areas of these shifting landscape types. Using tethersonde measurements at the coast of Kongsfjorden close to Ny-Ålesund, Argentini et al. (2003) found that the wind field and the thermal structure of the boundary layer is strongly influenced by the topography. Although the geostrophic wind direction matters for the flow strength, it was found that the direction of the local wind can not always be determined based on the overall wind direction. An analysis of near-surface turbulence and wind profile data performed by Kilpeläinen & Sjöblom (2010), using measurements conducted at the shore of Isfjorden, showed that momentum and sensible heat exchange is different in a fjord system than over the open ocean, as a result of the surrounding topography. In a study modelling the atmospheric variability over three different Svalbard fjords, Kilpeläinen et al. (2011) concluded that the complex shape of Isfjorden hinders effective spreading of air masses into the side branches, e.g. for air entering the fjord from the ocean. These spatial characteristics results in high spatial variability in meteorological variables. According to the authors, the spatial variability is large over all fjords and the surface type was mentioned as an important impact factor for the local conditions. Although studies have been done on e.g. sea ice extent (Serreze et al. 2007, Muckenhuber et al. 2016, Dahlke et al. 2020), inversions and low level jets (Vihma et al. 2011, Kilpeläinen et al. 2012, Palo et al. 2017) and small-scale heat exchange (Kilpeläinen & Sjöblom 2010, Jocher et al. 2012) in Arctic fjords, a commonly occurring statement in the literature is the fact that more observations and research is needed in order to better understand the unique characteristics of meteorological patterns in said landscapes.

This study contributes to the field of research with new knowledge and understanding of local- and microscale weather patterns over Isfjorden, Svalbard. The aim was to investigate the spatial variations in the three major atmospheric near-surface variables temperature, specific humidity and wind speed over the fjord. Data was studied from mobile automatic weather stations mounted onto tourist cruise ships, crossing Isfjorden on a more or less daily basis. As reference, data from a stationary automatic weather station situated at the northern coast of the fjord was used. The main questions addressed in the study are:

- Which spatial patterns in temperature, specific humidity and wind speed can be iden-

tified over Isfjorden? Can they be quantified?

- Can these patterns be connected to local factors such as surface cover and topography?

- Can these patterns be connected to the large-scale synoptic situation?

The present study aiming to answer these questions is structured in the following way: Section 2 introduces the reader to relevant meteorological concepts and their relevance in Arctic fjords. In Section 3, the study area of Isfjorden and instrumentational setup are presented. Methods for data handling and analyses used in this thesis are described. In Section 4, the results and analysis of the data are presented and discussed. In Section 5, the methods used in the study are assessed and discussed. In Section 6, conclusions of the study are summarized. Section 7 suggests future research on the topic.

2 Meteorological Theory

In order to interpret the spatial atmospheric variability, it is important to understand the physical processes that impact the relevant variables. In this study, the distribution of temperature, humidity, and wind speed, related to wind direction and seasonal change were investigated. Mathematical expressions describing the change in said variables over time are therefore presented in the following Sections 2.1 and 2.2.

2.1 Thermodynamics

2.1.1 Temperature

All motion and processes in the atmosphere are related to input of, change in and interaction between microscopic and macroscopic energy transfers (Stull 2017). The kinetic energy of molecular movement is what we call sensible heat (or enthalpy) and is what we measure as temperature. On the same microscopic scale, potential energy drives the changes in the binding structures of atoms and molecules, meaning that energy from a system can be absorbed or released, for example as latent bindings between molecules change (phase transitions). When evaporation of water occurs, the water changes from the liquid phase to gas phase. The addition of water vapor into the atmosphere increases the humidity of the air parcel interacting with the surface (described more in detail in Section 2.1.2). During this increase of the air parcel's moisture content, a latent heat flux is directed from the surface to the air. Heat can also be transferred between an air parcel and surrounding air through entrainment or detrainment caused by turbulent eddies, emittance of radiation, as well as conduction.

Considering a fixed location, the temperature change over time is dependent on the (temperature) gradient across the fixed volume studied. If the outgoing heat flux is smaller than the incoming (if the heat flux decreases across the dimensions of the volume), the temperature will increase over time – heat flux convergence. Consequently, the temperature change in the coordinate system can be described by Equation 1 (Stull 2017).

$$\frac{\partial T}{\partial t} = -\frac{1}{C_p \cdot \rho} \cdot \left[\frac{\partial \mathbf{F}_x}{\partial x} + \frac{\partial \mathbf{F}_y}{\partial y} + \frac{\partial \mathbf{F}_z}{\partial z}\right] + \frac{S_0}{C_p \cdot dt} \tag{1}$$

Here, C_p is the specific heat of air at constant pressure, ρ is air density, $\mathbf{F}$ is heat flux and S_0 is entropy. The first term on the right hand side of the equation stems from the first law of thermodynamics and the ideal gas law. The last term that includes the entropy change over time describes heat addition from sources within the air parcel itself.

Introducing a kinetic heat flux as $\frac{\mathbf{F}}{C_p \cdot \rho}$, simplifies Equation 1 to Equation 2 (Stull 2017).

$$\frac{\partial T}{\partial t} = -\left[\frac{\partial F_x}{\partial x} + \frac{\partial F_y}{\partial y} + \frac{\partial F_z}{\partial z}\right] + \frac{S_0}{C_p \cdot dt} \tag{2}$$

The kinetic heat flux F in each direction a includes contribution from different physical processes, such as advection (transportation by mass motion), conduction, radiation and

turbulent transport. With insertion of the expressions for heat fluxes for the most important contributions (horizontal advection by the mean wind, long-wave radiative heating and turbulent fluxes), and neglecting the contributions of magnitudes small enough to not be important, the air temperature change can be approximated with a simpler Eulerian net heat-budget equation (Stull 2017).

$$\frac{\partial T}{\partial t} = -[U \cdot \frac{\partial T}{\partial x} + V \cdot \frac{\partial T}{\partial y}] - \frac{\partial F_{z_{rad}}}{\partial z} - \frac{\partial F_{z_{turb}}(\theta)}{\partial z} + \frac{L_v}{C_p \cdot m_{air}} \cdot \frac{dm_{condens}}{dt} \tag{3}$$

U and V are the horizontal components of the wind vector in the x and y directions, ∂T is temperature change over distances x and y, $\frac{\partial F}{\partial z}$ is the heat flux gradient, $\frac{L_v}{C_p}$ is the latent to specific heat ratio, $m_{condens}$ is the mass of condensing liquid per mass unit of air, m_{air}, and time t.

2.1.2 Humidity

Humidity is a measure of how much water vapor an air mass contains and can be described using different quantities. For each air mass and its characteristics, a critical concentration of water vapor exists (Stull 2017). As the critical concentration, and therefore the saturation vapor pressure is reached, condensation happens faster than evaporation of liquid water. The air is said to be saturated when the vapor reaches this concentration. Saturation can be reached either through increasing the water vapor content of an air parcel (increase of the partial pressure from water vapor) or cooling the air parcel to the dew point temperature (a temperature value specific for the air mass properties', under which condensation occur) of an air parcel, according to an approximation described by the Clausius-Clapeyron equation (Stull 2017).

$$e_s \approx e_0 \cdot \exp[\frac{L}{R_v} \cdot (\frac{1}{T_0} - \frac{1}{T})] \tag{4}$$

e_s is the saturation vapor pressure, L is a latent heat parameter, R_v is the water-vapor gas constant, e_0 equals 6.11 hPa and T_0 equals 273.15 K.

It is also broadly accepted to use the August–Roche–Magnus formula, see Equation 5, to approximate the saturation vapor pressure, which avoids the issue of the latent heat parameter being dependent on temperature (Stull 2017).

$$e_s \approx 6.11 \cdot \exp[\frac{17.62 \cdot T}{T + 243.04}] \tag{5}$$

In Equation 5, the temperature should be given in degrees Celsius, not Kelvin. The approximated relationship is also presented in Figure 1.
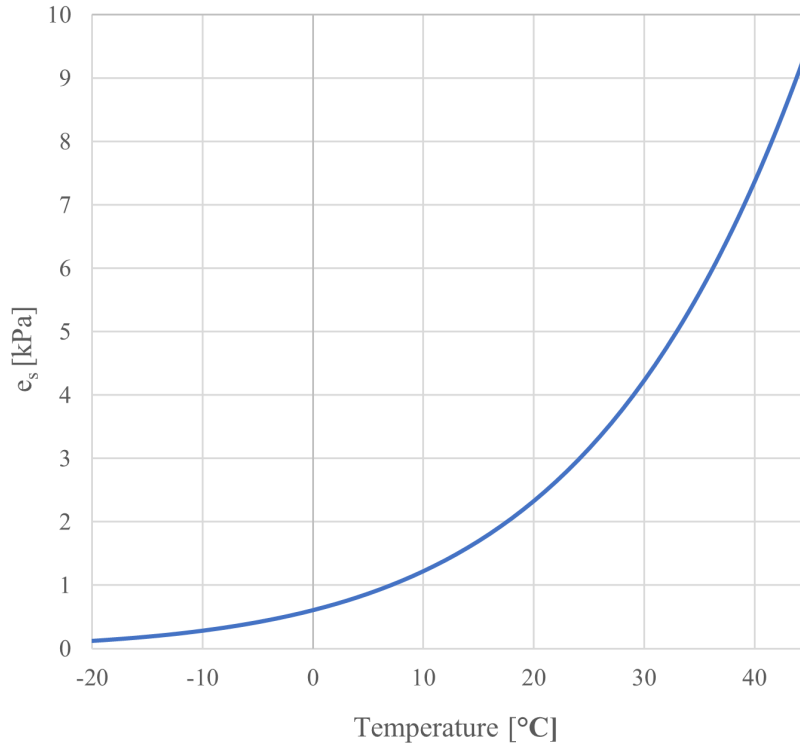
Figure 1: Relation between the saturation vapor pressure of pure water and temperature over a flat water surface.

The humidity of an air parcel can be quantified in numerous ways. Most commonly, relative and specific humidity are used. Relative humidity is the ratio between the prevailing vapor pressure and the saturation vapor pressure, and is strongly related to the temperature of the air mass, as explained by the Clausius-Clapeyron equation. Thus, the relative humidity of an air mass with constant water vapor concentration increases as the air is cooled.

Specific humidity is the mass of water per mass unit of air. It does not depend on other meteorological variables and is a feasible measure when studying variations over different dimensions, as the temperature dependency of relative humidity might inhibit the analysis of the humidity variable itself. The specific humidity can be calculated from the saturation vapor pressure and the over all air pressure, (p), see Equation 6.

$$q \approx \left(\frac{0.622 \cdot e}{p - 0.378 \cdot e} \right) \tag{6}$$

When the air becomes saturated, cloud or fog forms. The air then contains droplets and ice crystals suspended in the air. Clouds take different shapes depending on the physical processes behind their formation, while the characteristics of fog are primarily impacted by turbulent transport from the ground. As clouds take form, impact the overall atmospheric state as they reflect incoming solar radiation, while absorbing and re-emitting terrestrial radiation from the ground and the surrounding atmosphere.

2.1.3 Sensible and Latent Heat Fluxes

As shown in Equation 3, air temperature change over time depends, among other factors, on the flux of sensible heat. The specific humidity in the atmosphere is in turn affected by the evaporation occurring from the underlying surface. These sensible and latent heat fluxes are components in the surface energy balance (SEB).

$$R_N = S_{in} - S_{ref} + L_{in} - L_{out} = H_S + H_L + H_G \tag{7}$$

R_N is the net radiation, S_{in} is the incoming shortwave radiation, S_{ref} is the reflected short-wave radiation ($S_{in} \cdot \alpha$, where α is the surface albedo), L_{in} is the incoming longwave radiation, and L_{out} is the outgoing longwave radiation. H_S is the sensible heat flux, H_L is the latent heat flux and H_G is the ground heat flux.

The ratio of sensible to latent heat flux is known as the *Bowen Ratio* ($BR = \frac{H_S}{H_L}$), and as it describes how the radiative energy is partitioned into the two different turbulent fluxes, its value is closely related to the available amount of water of the underlying surface (dry areas are related to higher BR values than areas with more available water). The net radiation R_N is calculated by the radiation balance, see Equation 7.

2.2 Wind Dynamics

Just as any other fluid/body, air only moves as a result of net forces acting on it (Stull 2017). Atmospheric pressure at a certain height is a measure of the sum of the downward force (proportional to the mass) from all air molecules above. The impact of pressure can cause the molecules in the air mass to be compressed (density gets higher), and as the compression is the largest where the pressure is the highest, this takes place near the surface of the Earth. As a result, pressure decreases faster near the surface than at higher altitudes. The vertical pressure difference results in an upward directed pressure gradient force (PGF). On large scales, the vertical PGF is generally balanced by the gravitational force, a condition called the hydrostatical balance, see Equation 8 (Stull 2017).

$$\frac{\partial p}{\partial z} = -\rho(z) \cdot g \tag{8}$$

Pressure also decreases slower in warmer air temperatures compared to colder, as the molecules are further apart; the density (ρ) is lower, in that (the warmer) case. The relation between pressure, temperature and height can be described by Equation 9, which is the integrated form of Equation 8 (Stull 2017).

$$p(h) = p_0 \cdot e^{-\frac{mgh}{kT(h)}} \tag{9}$$

P_0 is the pressure at sea level (or another reference point), m is the molecular mass of air, g is the gravitational acceleration, h is height, k is the Boltzmann constant and T is the

temperature.

Horizontal pressure differences are fundamental to understand the origins of horizontal wind. In addition, the contributions of advection, centrifugal force, Coriolis force and turbulent drag are important for wind dynamics (Stull 2017). In regions where a horizontal pressure gradient resides, a force will be directed from high pressure to low pressure areas. The strength of this horizontal PGF depends on the the strength of the gradient, how great the pressure change is over a certain distance. As the PGF originates from a difference in applied forces, which is a necessity for acceleration (according to Newton's second law of motion), it is the only contribution that can initiate horizontal winds, while all other forces solely change the already prevailing wind speeds or directions.

Air masses can, in the same way as with e.g. enthalpy or humidity, carry specific momentum. Momentum is defined as mass times velocity, and specific momentum is defined as momentum per unit mass. As the definition of specific momentum indicates, partial air units within an air mass can have different velocity. Thus, the wind at a fixed point in space can change due to the difference in specific momentum prevailing within an air mass moving above the surface. This is called advection.

The centrifugal force is an inertial force, arising as a consequence of the air's acceleration in a rotating reference frame (over the surface of the Earth). The centrifugal force is apparent when an object rotates around a point, and is directed outwards from the center in the inertial reference frame.

The Coriolis force becomes apparent as an object, or in this case winds, moves along the rotational axis (of the Earth), following a curved path. The horizontal component of the centrifugal force will grow for higher latitudes, resulting in an unbalanced east-west component, defined as the Coriolis force. This result in all motions on the northern hemisphere getting deflected to the right and motions on the southern hemisphere getting deflected to the left.

The turbulence-drag force is caused by the roughness of the surface over which an air mass moves. As the air closest to the surface reaches obstructions, friction forces will act upon it and slow the wind down. States in the atmosphere where strong winds get slowed down close to the surface (wind sheer) are related to generation of mechanical turbulence near the ground surface. The near-surface turbulence further results in eddies impacting the winds higher up in the atmospheric boundary layer (ABL). The near-surface drag properties can also be transported up in the atmosphere through convection, which occur during periods of atmospheric instability.

In summary, the change in horizontal wind motions can be described by Equation 10 (Stull 2017).

$$\frac{\partial U}{\partial t} = -[U \cdot \frac{\partial U}{\partial x} - V \cdot \frac{\partial U}{\partial y} - W \cdot \frac{\partial U}{\partial z}] - \frac{1}{\rho} \cdot \frac{\partial P}{\partial x} + f_c \cdot V - w_T \cdot \frac{\partial U}{\partial z_i}$$
$$\frac{\partial V}{\partial t} = -[U \cdot \frac{\partial V}{\partial x} - V \cdot \frac{\partial V}{\partial y} - W \cdot \frac{\partial V}{\partial z}] - \frac{1}{\rho} \cdot \frac{\partial P}{\partial y} + f_c \cdot U - w_T \cdot \frac{\partial V}{\partial z_i} \tag{10}$$

The first three terms (where U, V and W are wind speed magnitudes in the directions x, y and z) describe the change due to advection, the next term describes the contribution of the pressure gradient, followed by the Coriolis force term (not discussed in detail here) and the turbulent drag term (where w_T is turbulent transport velocity). The centrifugal force is left out.

2.3 Meteorological Patterns over Arctic Fjords

2.3.1 Temperature

The surface cover characteristics for Svalbard include underlying permafrost and permanent snow and ice covering approximately 60% of the surface, which greatly impacts the local temperature distribution of the region (Sjöblom 2014). As shown in Equations 3 and 7, heat fluxes to the atmosphere are connected e.g. to the portion of incoming solar radiation that gets reflected (S_{ref}), which is expressed as the surface albedo. Snow and ice have higher albedo values than open water and land, which impacts the net radiation (R_N) and possibly limits the magnitude of heat fluxes to the atmosphere (in comparison to the same conditions over bare land and open water). The ratio between sensible and latent heat fluxes (described by the BR, see Section 2.1.3) depends on the water content of the ground. A study by Westermann et al. (2011) based on high resolution thermal imaging close to Ny-Ålseund, Svalbard, showed differences of 10 K in instantaneous air temperatures values over wet (colder) respectively dry (warmer) surfaces. These maximum values were reached during times of high absolute values in net radiation and clear sky conditions. These processes collectively are fundamental for the surface temperature, which determines the emitted longwave radiation (L_{out} in Equation 7) to the atmosphere. The surface temperature also contributes to the strength of the vertical temperature gradient (which forces the sensible heat flux, H_S in Equation 7).

In the Arctic regions, radiative fluxes play a particularly important role in the ABL's thermal structure during the polar night (as S_{in} in Equation 7 is then equal to zero). The heat loss due to outgoing longwave radiation cause strong near-surface inversions in the atmosphere (Jocher et al. 2012). Characteristic for temperature inversion layers is that the temperature increases with height, creates a state of strong stability in the atmosphere as vertical movement is inhibited. Using data from tethersonde measurements Characteristic for temperature inversion layers is that the temperature increases with height, , Vihma et al. (2011) found that temperature inversions over the coast of Isfjorden are the strongest in relatively warm and moist air masses, presumably due to breakage in cloud cover which enhances surface cooling (as a result of reduced L_{in} in Equation 7). In general, high wind speeds coincide with weaker and more elevated inversions, as mixing erodes the inversion layer. However,

the strongest temperature inversion developed during the measuring period appeared when cold air was advected near the surface by strong katabatic flows. Palo et al. (2017) also analyzed tethersonde data, in this case from a station drifting in the Arctic Ocean from April to August 2007. They concluded that warm-air advection and melting processes are more important than radiative fluxes for summer temperature inversions over sea ice in the central Arctic. The strongest inversions, according to (Palo et al. 2017), were found during clear sky conditions.

It is also relevant to consider the relationship between air temperature and sea ice extent for studies of Arctic fjord systems. The western part of the Svalbard archipelago is influenced by the West Spitsbergen Current (WSC), a northern branch of the Gulf Stream transporting relatively warm water masses polewards. Thus, the sea ice in western Spitsbergen fjords does not have a history of being perennial (intact across the entire year) in contrast to the northern and eastern parts of the island (Dahlke et al. 2020). Instead, the extent of seasonal sea ice coverage in western fjords varies greatly from year to year (Muckenhuber et al. 2016). However, a coastal current of cold freshwater from river and glacier runoff follows the coast northward on the western side and separates the fjord water from the WSC and enables sea ice growth inside the fjords during winter (Muckenhuber et al. 2016). Exchange between the oceanic and fjord water depends on the density difference between the water masses (Nilsen et al. 2008). Though Dahlke et al. (2020) concluded that the variability in surface air temperature is driving the change in sea ice extent in Svalbard fjords on a large scale, rather than vice versa, the opposite has been found to be the case in other Arctic regions (Chen & Wu 2018, Deng & Dai 2022). It is, in any case, reasonable to assume that sea ice does have an impact on the air temperature on a small scale, as it changes local the physical surface characteristics. Sotiropoulou et al. (2016) provides a detailed comparison on the atmospheric conditions for open water and sea ice surfaces during the Arctic Clouds in Summer Experiment (ACSE) in 2014. The experiment took place over the summer and early autumn and measurements included vertical temperature profiling with radiosondes and cloud characterisation. It was found that the initiation of the autumn freezing processes are related to advection of cold air masses, rather than to solar radiation properties alone. The process was explained as a result of the cold-air advection over the water leading to heat extraction from the water surface, and further to freezing (Sotiropoulou et al. 2016).

2.3.2 Humidity

Variations in humidity content are, similarly to the temperature conditions discussed in Section 2.3.1, impacted by surface features (as the latent heat flux magnitude is limited by the net radiation, see Equation 7). Great net energy income (controlled by e.g. S_{ref} and L_{out}, both depending on the surface cover) enables greater forcing of a latent heat flux to the atmosphere. In addition, over water, addition of water vapor from evaporation could also be restricted by limited air-ocean interactions caused by local sea ice. During a tests of different observation techniques for turbulent fluxes of momentum and heat in Adventdalen, Sjöblom (2014) showed that the latent heat flux over land changes substantially during the summer, from being positive in early summer to negative in July and August (which would

result in an increased ground heat flux, H_G in Equation 7, over the summer). This finding differs from other studies where latent heat flux have been studied over surfaces with similar characteristics (Lloyd et al. 2001, Westermann et al. 2011). Measurements of heat and water vapor fluxes in Ny-Ålesund have, in contrast, shown that the latent heat flux over land increases over the summer, due to increasingly large proportions of the incoming energy going into thawing of the permafrost (Lloyd et al. 2001). These differing results further establish the importance of small-scale processes and differences for the local humidity distribution in the Svalbard region (Eugster et al. 2000, Sjöblom 2014). As mentioned in Section 2.1.3, the available water content controls the division of sensible and latent heat fluxes in the SEB. Wet areas are related to lower BR values, as larger proportion of the net energy goes into evaporation than sensible heating. A comparison of BR values over a drained tundra area and a control area in northeast Siberia, conducted by Göckede et al. (2017), showed an increase of 18% in the BR over the course of the drainage process. The water content is especially important when studying the atmosphere above a water surface such as Isfjorden, where the water availability on a small scale is unlimited. Moreover, the water vapor content of the air advected from over land depends on the surface cover from where it origins.

The relatively cold temperatures in the Arctic will limit the strength of specific humidity gradients (forcing H_L in Equation 7), as the differences between saturated vapor pressures are relatively small between different temperatures below freezing, see Figure 1. As the vapor pressure decides the specific humidity, see Equation 6, and neither the surface nor the atmosphere will reach vapor pressure values above e_s, greater specific humidity gradients between the surface and atmosphere are expected during the warmer seasons compared to the colder seasons.

As for temperature, inversion layers are known to occur for specific humidity. Sotiropoulou et al. (2016) found that deeper specific humidity inversions occur over the sea ice (due to warm and moist air advection higher up in the ABL) than over open water (due to buoyant fluxes, initiated by heat extraction from the water to the atmosphere) during the summer. The strongest humidity inversions were found over melting sea ice, possibly as a result of increased available water for evaporation over the surface after melting. It is important to note that the humidity inversion only tells us how the specific humidity varies with height through the ABL, and the inversion strength does not measure the absolute water vapor content in the air.

2.3.3 Wind Dynamics

The main wind direction is E-SE in the area of the Svalbard archipelago. Although the main flow is forced by semi-permanent pressure systems, local air flows are often related to factors such as topography and diversity in surface cover (Przybylak 2016, Wickström et al. 2020). For fjords that are partly ice-free, such as Isfjorden during the majority of the year, the differences of heat fluxes (mentioned in Sections 2.3.1 and 2.3.2) as well as the shifting roughness over the fjord may further impact the air flow (Vihma et al. 2011). Channeled flow, where the air mass is constrained on both sides by e.g. mountains, can be thermally

driven, pressure driven or mechanically forced (Whiteman & Doran 1993, Esau & Repina 2012, Nawri & Harstveit 2012). These different types of channeling are further discussed in the following paragraphs.

Thermally driven flows become apparent when geostrophic winds are low, as pressure gradients in the valley occur due to temperature differences (described by Equations 8 and 9). The impact of this process is especially essential in valleys connecting different surfaces such as land and water, over which the temperatures may substantially differ (as discussed in Section 2.3.1). In the Arctic regions, this process primarily occurs during the polar night as the temperature difference over land and the fjord then is the greatest, and might result in outflow of the fjord valleys in the form of land-breezes (Esau & Repina 2012, Kitowska et al. 2021). Further, in combination with the PGF, the cooling from the ground higher up in the terrain result in gravitational drainage winds, so-called katabatic winds, of the dense air down the valleys (Argentini et al. 2003, Kazanskii 2010). In a study comparing the results from the Weather Research and Forecasting (WRF) mesoscale model with measurements from tower observations and radiosoundings, Kilpeläinen et al. (2011) found that the role of topography is greater than the role of different surface type, regarding the extent of spatial wind speed variability over Isfjorden. However, as Esau & Repina (2012) and Kitowska et al. (2021) studied wind forcing mechanisms from observation data and simulations respectively, they concluded that temperature differences are the primary driver for valley flows around Kongsfjorden and Hornsund in Svalbard. Regardless, the PGF and the gravitational force are both known to result in outflow from surrounding glaciers, down over the fjords, in the Svalbard region.

If the valley winds are driven by (and aligned with) the pressure gradient component of the geostrophic wind, the channeling effect is said to be pressure driven (Nawri & Harstveit 2012). When the geostrophic wind is directed parallell to the valley axis, the along-valley component will be equal to zero (as geostrophic wind is defined as balanced by the PGF and Coriolis force, mentioned in Section 2.2). For all other cases, a pressure difference will prevail along the fjord's axis and can induce an air flow through the valley. In cases where the pressure gradient component is aligned in opposition to the along-valley wind direction, counter currents might be generated (Whiteman & Doran 1993).

Forced channeling occurs when winds aloft (the valley) are aligned with the valley's axis (Whiteman & Doran 1993). This type of channeling process is especially prominent in narrow valleys with high sides. Valley wind can also be induced by downward transport of momentum from aloft. When studying the connections between local surface wind variability in Finnmark (northern Norway) and the larger-scale atmospheric circulation, Nawri & Harstveit (2012) found that downward mixing of overlying winds is more prominent during summer than winter, as the stable stratification of the boundary layer decreased during summer due to increased incoming solar radiation. However, for observations in valleys, wind directions aligned with the valley's axis dominated and coincided with the direction of prevailing temperature gradients along the fjord (Nawri & Harstveit 2012).

3 Methods

For the purpose of reaching the goals stated in Section 1, meteorological variables over Isfjorden, Svalbard were analyzed using measurements from mobile and stationary weather stations. The study area characteristics are described in Section 3.1, followed by descriptions of the instrumentation and setup in Section 3.2. Section 3.2.1 covers the instrumentation used for the measurements. The weather station networks are introduced in Section 3.2.2 (for the mobile network) and Sections 3.2.3 and 3.2.4 (for the stationary network). Lastly, the data handling process is described in Section 3.3, including correction for land fetch impact on the reference data in Section 3.3.1, preprocessing in Section 3.3.2 and filtering in Section 3.3.3.

3.1 Area

Spitsbergen is the biggest island of the Svalbard archipelago, situated north of the Norwegian Sea between 76 and 80°N, and 10 and 28°E. For this study, measurements were performed across and around Isfjorden, the largest fjord on Spitsbergen, see Figure 2.

Isfjorden is situated on the west coast of the island and is approximately 20 km wide. It cuts over 100 km into the island in the northeastern direction, with its mouth opening to the Fram Strait at the southwest end and branches making up Dicksonfjorden and Billefjorden furthest to the northeast. The landscape around the mouth is embossed by rounded mountains and bedrock. Further east into the fjord, following the south side, most of the landscape is made up by plateau-shaped mountains characteristic for Spitsbergen. The height of the plateaus are generally between 400 and 600 m above sea level, with some exceptions. The mountains along the fjord coast are particularly high furthest east into the fjord, around the mouth of Billefjorden and Tempelfjorden, where the peaks are close to 800 m above sea level and the mountain sides are particularly steep. The northern shores of Isfjorden is dominated by large marine-terminating glaciers. Additional fjord branches include Sassenfjorden and Adventfjorden. Longyearbyen, the main settlement in the archipelago and home to the majority of Svalbard's population, is situated at the southern side of Adventfjorden.

Figure 2: Overview map of the study area Isfjorden, on the west coast of Spitsbergen in the Svalbard archipelago. Marked in the map are populated settlements, positions of the stationary weather stations and main areas discussed in this project.

3.2 Instrumentation and Setup

In order to obtain atmospheric measurements throughout Isfjorden for the spatial variability analysis, the automatic weather station MaxiMet GMX500 (described in Section 3.2.1) was installed at three different ships crossing the fjord (see Section 3.2.2) and programmed to log data at 1 min resolution. As it was found that a stationary reference was needed (see Section 3.2.3), data of the same temporal resolution was also used from Bohemanneset lighthouse (measured by the MaxiMet GMX500) as well as Avinor's and the Norwegian Meteorological Institute's weather station at Longyearbyen (LYR) airport (see Section 3.2.4).

3.2.1 MaxiMet GMX500 Automatic Weather Station

The automatic weather stations (AWS) used in this project were MaxiMet GMX500, designed and manufactured by Gill Instruments Limited. The stations are 22 cm high, have a 14 cm diameter and are covered with a multi-plate solar radiation shield to prevent errors

caused by solar radiation (see Figure 13 in Appendix A). Temperature and relative humidity measurements are conducted using an internal solid state sensor circuit and wind measurements are conducted through an ultrasonic sensor. A sound pulse is sent from the north to the south transducer, before a pulse is sent in the opposite direction (and similarly for the eastern and western directions). Wind speed and direction can then be calculated from the difference between the signal travel times in each direction. See Table 1 for accuracy specifications of the sensors.

Table 1: Accuracy of the meteorological parameters measured by the MaxiMet GMX500

Parameter	Accuracy
Temperature	$\pm 0.3°$C @ 20°C
Humidity	$\pm 2\%$ @ 20°C
Pressure	± 0.5 hPa @ 25°C
Wind Direction	$\pm 3°$ up to 40 m/s
Wind Speed	$\pm 3\%$ up to 40 m/s

To ensure correct wind direction measurements, the MaxiMet GMX500 at Bohemanneset (BHN), see Figure 2, was adjusted with the north alignment pointer (marked on the station) in the northern direction. The mobile stations were, naturally, not always facing north and the speed of the ship additionally disturbed the wind speed measurements. To correct the raw wind parameters measured at the mobile stations, the wind components were first calculated from the raw wind speed and direction output, see Equation 11.

$$
\begin{aligned}
U_{raw} &= -ws_{raw} \cdot sin(\theta_{raw}) \\
V_{raw} &= -ws_{raw} \cdot cos(\theta_{raw})
\end{aligned}
\tag{11}
$$

U_{raw} and V_{raw} are the wind components, ws_{raw} is the measured wind speed and θ_{raw} is the measured wind direction (relative to the sensor). The applied contribution from the movement of the ship were then calculated in similar ways, see Equation 12.

$$
\begin{aligned}
V_{xship} &= -V_{GPS} \cdot sin(\theta_{GPS}) \\
V_{yship} &= -V_{GPS} \cdot cos(\theta_{GPS})
\end{aligned}
\tag{12}
$$

V_{xship} and V_{yship} are the ship speed magnitudes in the x and y directions, V_{GPS} is the speed of the GPS (given as an output from the AWS, based on the distance over time) and θ_{GPS} is the heading of the ship (also given as an output). After the applied wind speed from the ship's movement was subtracted from the measured wind in each direction, the correct wind speed magnitude and direction were calculated from the corrected components, see Equations 13, 14 and 15.

$$
\begin{aligned}
U_{corr} &= U_{raw} - V_{xship} \\
V_{corr} &= V_{raw} - V_{yship}
\end{aligned}
\tag{13}
$$

$$ws = \sqrt{U_{corr}^2 + V_{corr}^2} \tag{14}$$

$$\theta = arctan(\frac{V_{corr}}{U_{corr}}) \tag{15}$$

ws is the wind speed, θ is the wind direction, U_{corr} and V_{corr} are the corrected wind speed compontents.

3.2.2 Mobile Weather Station Network

To obtain atmospheric measurements from varying spatial conditions all over the fjord, MaxiMet GMX500's (logging their positions) were installed at three tourist ships (see Figure 3). The ships carried out daily cruises across Isfjorden and consistently measured along the way. They were included due to their regular cruising schedules and tracks, which allowed for rich amounts of data throughout the fjord during the seasons they operated in the Svalbard region. Most commonly they visited the coal-mining town Barentsburg (southwest along the coast from Longyearbyen) and Pyramiden in Billefjorden (furthest to the northeast in Isfjorden), see Figure 2. As seen in the data presented in Section 4, the destinations of the cruises differed slightly over the cruising season, and measurements were also conducted in Borebukta, Ymerbukta and Trygghamna, southwest along the coast from Bohemanflya.

MS Polargirl, owned by the company Polarcharter (to the far left in Figure 3), is a 39 meters long and 8 meters wide, streamlined passenger ship built in 1962 (Polarcharter n.d.). The weather station was mounted at a beam on the highest point of the mast, to minimize disturbances in the measurement caused by the shape of the ship, at approximately 18 m asl. MS Billefjord is a 35 meters long and 8 m wide passenger ship built in 1986 (in the middle at Figure 3). The ship has streamline shape (Vesselfinder n.d.). The weather station was positioned similarly as at MS Polargirl, at around 17 m asl, at the highest point of the mast. MS Bard is a 11 meters wide and 24 meters long hybrid-electric catamaran (BrimExplorer n.d.), to the far right in Figure 3. The weather station was placed at a beam on the bridge, at approximately the same height as for the other ships, at the highest point of the vessel (see Figure 4).

Figure 3: From the left: MS Polargirl, MS Billefjord and MS Bard (in the Longyearbyen harbour). Position of the mobile AWS's on the ships are marked with arrows.
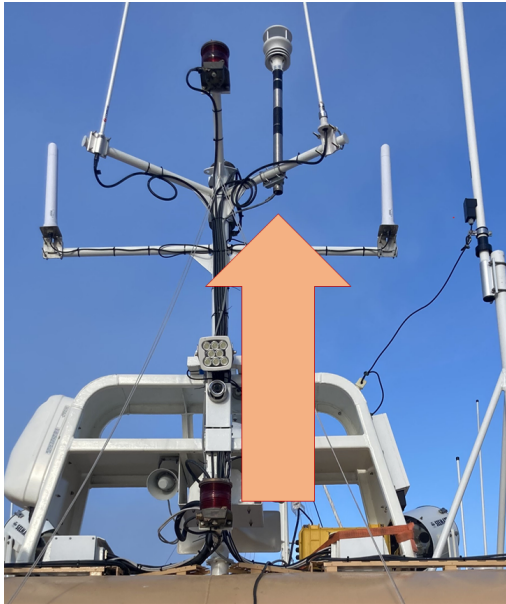

Figure 4: Setup of AWS on a pole, attached to a beam at the bridge of MS Bard. Arrow points at the AWS (MaxiMet GMX500).

Measurements were performed at MS Billefjord between the 20th of March and 31st of August

2022, at MS Polargirl from 30th of May until October 2022, and at MS Bard from the 5th of May 2022 until October 2022, see Figure 5.
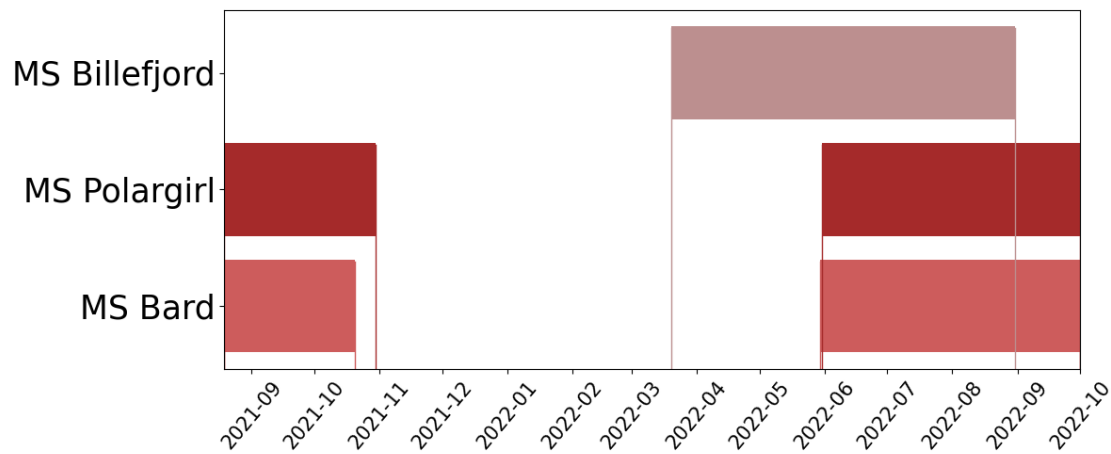
Figure 5: Timeline for data collection from the mobile AWS, at the three different ships, used in this study

The AWS's in the mobile network scans for meteorological parameter values every second and the data is logged either as momentary samples or averages, maximum or minimum values over a specified temporal resolution. The configuration of the data from the mobile AWS network during two different time periods is presented in Table 2.

Table 2: Measured parameters and their processing from the mobile AWS's followed the form presented in the upper part of the table until the 5th of May 2022. In order to standardize the data, the configuration was changed to the arrangement shown in the lower part of the table. *AmbTemp* is ambient temperature, *RelHum* is relative humidity, *SensorDP* is sensor dew point, *BarP* is barometric pressure, *GPSLoc* is GPS location, *WS* is wind speed and *WD* is wind direction (both raw and corrected values for the wind parameters)

Before the 5th of May 2022							
Scan interval: 1 s. Output time intervals: 20 s, 1 min, 5 min, 10 min, 1 h.							
	AmbTemp	RelHum	SensorDP	BarP	GPSLoc	WS	WD
Sample	X	X	X	X	X		
Average						X	
Maximum	X	X				X	X
Minimum	X	X					
After the 5th of May 2022							
Scan interval: 1 s. Output time intervals: 20 s, 1 min, 10 min.							
	AmbTemp	RelHum	SensorDP	BarP	GPSLoc	WS	WD
Sample	X	X			X	X	X
Average	X	X	X	X		X	X
Maximum						X	
Minimum							

3.2.3 Bohemanneset Station

Although the measurements from the mobile network generated an overview of the meteorological conditions throughout the fjord, the goal was to investigate solely the spatial variability of the variables. Therefore, it was necessary to eliminate the impact on the measurements from synoptic-scale processes and temporal factors (such as the diurnal cycle of incoming solar radiation). Only the observed perturbations (in relation to the overall prevailing conditions over Isfjorden), due to spatial factors such as topography and surface cover, were considered relevant.

To obtain reference values describing the large-scale temporal change in meteorological variables over the fjord, a stationary automatic weather station was installed at the lighthouse at Bohemanneset (BHN), see Figure 2. The position is favorable to use for measurements meant to reflect the ambient fjord conditions, as the BHN lighthouse is located relatively far away from disturbing terrain. The land around the station is relatively flat, as BHN is the southeastern isthmus of the Bohemanflya peninsula, a plain land sticking out around 10 km into Isfjorden in the southeastern direction. The lighthouse is surrounded by water from three sides,with exception of the northwestern direction. The station was operational from 18th of August 2021 and is powered by a 15 V battery, charged by solar panels mounted on the lighthouse, with the primary purpose of powering the light. The station is mounted on the top of the lighthouse (see Figure 6). Cables for power and data transferring goes through a hole in the roof, into the lighthouse where a logger box is placed. The height of the station is approximately 4 meters asl.

Figure 6: Setup of AWS on a pole, attached to the roof on a lighthouse. Arrow points at the AWS (MaxiMet GMX500).

The AWS scans for meteorological parameter values every five seconds and the data is either logged as samples (momentary values) or averages, maximum or minimum values (over a specified time period). The configuration of the data from the BHN station is presented in Table 3.

Table 3: Measured parameters and their processing from the AWS station at BHN followed the form presented in the upper part of the table until the 5th of May 2022. In order to standardize the data, the configuration was changed to the arrangement shown in the lower part of the table. *AmbTemp* is ambient temperature, *RelHum* is relative humidity, *SensorDP* is sensor dew point, *BarP* is barometric pressure, *WS* is wind speed and *WD* is wind direction (for the wind parameters, both raw and corrected values were obtained).

Until the 5th of May 2022						
Scan interval: 5 s. Output time intervals: 1 min, 10 min, 1 h.						
	AmbTemp	RelHum	SensorDP	BarP	WS	WD
Sample	X	X	X	X	X	X
Average		X		X	X	
Maximum	X				X	
Minimum	X				X	
After the 5th of May 2022						
Scan interval: 5 s. Output time intervals: 1 min, 10 min.						
	AmbTemp	RelHum	SensorDP	BarP	WS	WD
Sample						
Average	X	X	X	X	X	X
Maximum					X	
Minimum						

3.2.4 Longyearbyen Airport Station

When studying the 2021 time series measured at BHN, a connection was found between sudden wind direction changes and peaks or drops in temperature, relative humidity and wind speed values. The variables' dependency on wind direction indicated different impact of the underlying surfaces for when the air was advected from over land or from over sea, so-called fetch. This is problematic as the intention was to use measurements at BHN as a reference station for the ambient conditions over Isfjorden. Thus, only the water fetch was considered interesting and a correction was needed for the times when the stationary data values were impacted by land fetch. To account for this, a correction (described in detail in Section 3.3.1) was applied to the BHN data set using data from an other stationary weather station at Longyearbyen airport.

To avoid the impact of land fetch in the stationary data set, 30 min (or hourly, depending on the season and parameter) data from a weather station owned by the Norwegian Meteorological Institute and Avinor, located at the airport close to Longyearbyen was used for correction (see Section 3.3.1).

The weather station was established in 1964 and is situated at 28 m asl on the southwestern side of the runway, with Platåberget mountain in the southern direction and Adventfjorden in the northern direction (Met.no n.d.). The station is located approximately 1 km in from the Isfjorden shore (in the NW direction, see Figure 2), but it was assumed that the air

there would have experienced less impact of the underneath land surface than the air mass measured at BHN during the same wind conditions.

3.3 Data Handling

To correct for land-fetch mentioned in previous paragraph, a weighting function was applied to the stationary data sets, see Section 3.3.1. In order to prepare the data for calculation of spatial anomalies of the meteorological variables, the data was preprocessed (see Section 3.3.2) and to enable analysis of impact parameters on the variability, the data was filtered into categories based on the prevailing conditions during which the measurements took place (see Section 3.3.3).

3.3.1 Stationary Data Set Correction

As mentioned in Section 3.2.3, it was found that the temperature, relative humidity and wind speed measurements were impacted by land fetch during certain prevailing wind directions. In order to find wind sector limits for when the air flow changed to advection from over land, the wind direction before and after particularly large jumps in the temperature data were noted. The wind directions were further plotted as polar coordinates, with the center of the coordinate system at the position of the BHN weather station (see panel a in Figure 7). Directions corresponding to warmer temperatures were plotted in red and the colder ones in blue. The size of the markers indicate the magnitude of increase/decrease related to the wind direction switch. Figure 7 shows that the correction was needed for wind directions between 250° and 20°.

Instead of making a step, transitioning directly from BHN to LYR airport data over a singular unit in the wind direction range, a function was applied to the reference data set (see Equation 16). For the sector 270°-0°, only data from the airport station was used and for 20°-250°, only data from the BHN station was used (see panel b in Figure 7). For the sectors in between, the function weights the data values measured at the LYR airport station higher for wind directions closer to land and the values from the BHN station higher for directions closer to the water.
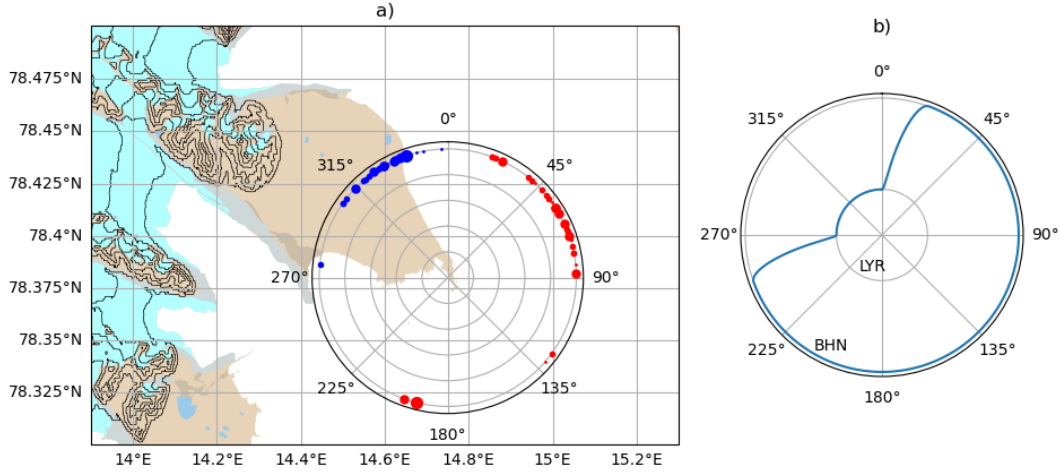
Figure 7: a) wind directions for which sudden drops/peaks in temperature, humidity and wind speed occurred. The red markers show the wind directions for which the temperature was relatively higher ("before a sudden drop") and blue markers for wind directions with lower temperature ("after a sudden drop"). Origo is placed over the location of the BHN weather station. b) the weighting function applied to the data values from BHN and LYR airport. The values in the graph represent the proportion of the value being from BHN; more towards BHN for higher values in the graph and more towards LYR airport for lower values in the graph. Between 20° and 250°, only data from BHN is used. Between 270° and 0°, only data from LYR airport is used. For the wind sectors in between, values from both stations are combined.

The developed weighting function is presented in panel b in Figure 7 and was, as mentioned, applied to the reference temperature, specific humidity, and wind speed data sets. The equation used is presented in Equation 16.

$$X = \alpha \cdot X_{BHN} + (1-\alpha) \cdot X_{LYR}$$

(16)

$$\alpha = \begin{cases} 1, & \text{if } 20° < wdir < 250° \\ 0, & \text{if } 270° < wdir < 0° \\ sin(wdir), & \text{if } 250° < wdir < 270° \\ sin(wdir - 270), & \text{if } 0° < wdir < 20° \end{cases}$$

$wdir$ is the measured wind direction, X is the meteorological variable value substracted from the mobile data measurements, X_{BHN} is the meteorological variable value measured at Bohemanneset and X_{LYR} is the meteorological variable value measured at Longyearbyen airport.

The data from the LYR airport had lower temporal resolution than the output data from the mobile AWS's. Thus, interpolation of the temperature, relative humidity and wind speed

30

values conducted at the LYR airport was necessary for removing the ambient values for every point in time (and make use of all measurements from the mobile AWS's). The LYR airport data set was resampled to 1 minute values by linear interpolation.

3.3.2 Preprocessing of Data

The aim of this study was (as mentioned in Section 1) to investigate the spatial variability in meteorological variables without the contribution of large-scale and temporal processes. To exclude all variations except those originating from local spatial characteristics, the values in the reference data set (which were regarded as measurements of the ambient fjord conditions) were subtracted from the values measured at the mobile stations for every point in time, leaving only the measured anomalies for the specific position and time.

Further, the ships were standing still in the harbours (in LYR, Barentsburg and Pyramiden) over substantial times during the measuring period, which generated large amounts of data that were not useful for the spatial variability investigation. Based on the limit longitude and latitude values, approximated on a map for the harbours, all measurements conducted when the ships in the harbours were removed from the mobile data sets.

Measured temperature and calculated specific humidity reference values were subtracted from the values in the mobile data set for every point in time. As absolute differences in wind speed are related to the initial speed (that is to say, a larger force is needed for the wind speed to increase from 1 to 2 m/s, than from 10 to 11 m/s, e.g.), the local wind speed relative to the reference was considered more interesting for the study. The wind speed ratio of the mobile measurement and reference was calculated (for every point in time) instead of the differences. These data sets, only containing the meteorological perturbations due to spatial differences, are further called the temperature, humidity and wind speed anomaly data sets.

3.3.3 Data Filtering

In order to perform statistical analysis of the meteorological parameters at certain areas of the fjord, the anomaly data was sorted into spatial grid-boxes over Isfjorden, see Figure 8. The extent of the grid was limited to the maximum and minimum latitude respective longitude values present in the data sets, and as the aim was to obtain a high spatial resolution resolving the variations over the different areas of the fjord, 50×50 square grid-boxes (corresponding to around 1×1 km) were used. An average value of all the anomaly data points within a grid-box was calculated, and could be plotted as a single value connected to the position of the measurement (over the specific grid-box extent) on a map.

In order to quantify the overall horizontal differences between inner and outer fjord, and to study them in combination with the difference in temperature between air and water over the measuring period, a more spatially coarse analysis was conducted as well. Only two grid-boxes of approximately 30×30 km were used to calculate the horizontal differences in temperature and humidity, as the analysis described in the previous paragraph showed that

31

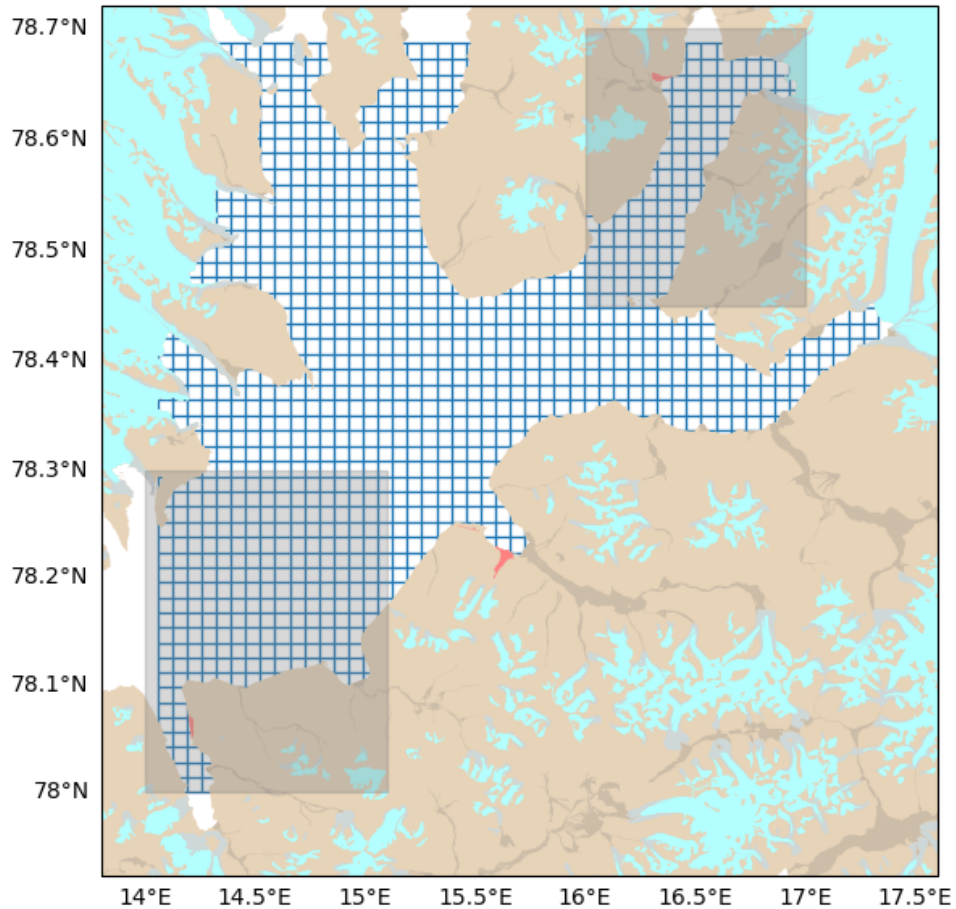a lower spatial resolution was sufficient to resolve the differences, see Figure 8.

Figure 8: Points showing the outer corners of every box in a 50×50 grid applied over Isfjorden. The anomaly data was sorted into respective grid-box, over which statistical analysis was conducted.

The variability in the temperature and specific humidity variables was expected to be impacted by e.g. the land-sea temperature gradient, sea ice extent, snow cover and ground water content, which are all factors that are changing over the seasons. In order to visualize said impacts, which would show as different spatial patterns during the different seasons, the temperature and specific humidity anomaly data sets were sorted into categories, based on the season during which the measurement was made. The seasons were chosen as March-May (spring), June-August (summer) and September-October (autumn).

The annual cycle was not expected to impact the local spatial wind speed variability in the same way as the thermodynamic variables. Rather, as the dynamics of the flow are related to the speed of the air, the magnitude of the ambient wind speed was considered relevant for the distribution of anomalies throughout Isfjorden. The wind speed anomaly data set was sorted into threshold categories corresponding to the proportion of the maximum wind speed over the entire period. The categories were chosen to data measured during 0-20% of the maximum wind speed value (0-3.2 m/s), 20-40% (3.2-6.4 m/s), 40-60% (6.4-9.6 m/s), 60-80% (9.6-12.8 m/s), and 80-100% (12.8-16 m/s). However, since the maximum measured wind speed value greatly exceeded the vast majority of the other wind speed values, the 99% quantile of the wind speed data was used instead of the actual maximum value.

The wind direction was considered relevant for all meteorological variables, as it might present the impact of advection from different surface covers and topography. Advection may impact both the thermodynamic and mechanic variables (as mention in Section 2), due to transport of heat, moisture and momentum characteristics. The fact that the wind flow can be (negatively or positively) accelerated due to the shape of the surface over which it travels, further makes the wind direction an important parameter regarding the local wind speed distribution. The anomaly data was therefore filtered into categories based on the prevailing ambient wind direction conditions at BHN during which the measurements were conducted. Through this data filtering process, the average spatial anomalies in the meteorological variables could be visualized in two dimensions (being the possible impacting factors).

To obtain a weekly average difference between the head and the mouth of the fjord, the weekly averages from the inner part of the fjord were substracted from the weekly averages from the outer (see Figure 8 for definitions of "inner" and "outer" parts of the fjord). In order to compare the weekly gradient strength with the air-water temperature gradient, ambient temperature measurements from BHN were substracted from sea surface temperature (SST) values. The SST was measured during CTD scans at the interdisciplinary Isfjorden Adventfjorden times series station (IsA) close to the mouth of Adventfjorden (Chitkara et. al, in prep). IsA was established in 2011, it is maintained by UNIS and sampling of biological and oceanographic parameters are conducted at the station on a monthly basis (UNIS n.d.).

4 Results and Discussion

In order to study the spatial patterns of the three major meteorological near-surface variables, averages (within each spatial grid-box) of anomaly data were plotted over Isfjorden. Temperature patterns are shown and discussed in Section 4.1.1, humidity patterns are showed and discussed in Section 4.1.2, and in Section 4.1.3 a synergy of both thermodynamic variables is presented. Wind speed patterns are covered in Section 4.2.

4.1 Temperature and Humidity Patterns

4.1.1 Spatial Temperature Distribution

Figure 9 shows spatial temperature anomaly distributions over Isfjorden, binned into categories of seasons (March-May for spring, June-August for summer and September-October for autumn) and wind directions. The number of data points in every grid-box is shown in Figure 14 in Appendix A.

A re-occurring temperature pattern during various seasons and wind directions is a gradient directed along the Isfjorden axis (see in Figure 9). In spring, the temperature gradient appears strongly during northerly wind directions, measuring a difference of around 3-3.5°C between Isfjorden's innermost (colder) and outermost (warmer) parts. For E winds, the temperature difference is roughly 1°C between the fjord's inner and outer parts. No data is available from the outermost part of Isfjorden during SE and S wind in the same time period, however a gradient is still visible over the part of the fjord from which data exists. During the summer, the horizontal gradient is weaker; around 1°C for NW and SE winds. For the remaining wind directions, the temperature is homogeneously colder all over the fjord, relative to the reference station. During S and SW wind directions in summer, the gradient is reversed compared to the one in spring and autumn, while the difference between the inner and outer part still measures values of around 1°C. In autumn, the anomaly difference increases compared to summer, but does not reach the same magnitudes as those seen in spring. Horizontal differences (with a warmer area closer to the mouth and vice versa) of 1-2°C can be seen in autumn during all wind directions except W and NW winds, were the temperature anomaly values are more or less constant along the fjord.
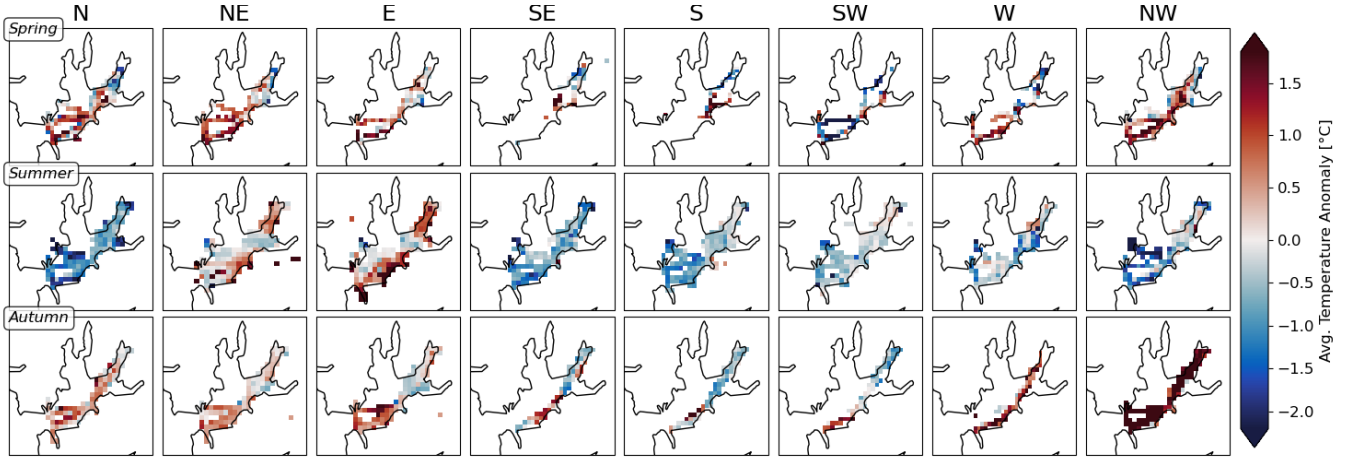
Figure 9: Spatial distribution of mean temperature anomalies during different seasons (rows) and wind directions (columns).

Different factors contribute to the temperature gradient, out of which some are not related to the wind direction. In March and April, the innermost part of Isfjorden was covered by sea ice. Although the sea ice had mostly melted in May, it is still reasonable to assume that some drift ice resided in the fjord at that time. As ice has a higher albedo than open water, a larger proportion of downward solar radiation is reflected and less energy is available to heat up the water surface and onwards the atmosphere. In summer, the ice-free water surface results in a more homogeneous temperature distribution (than in spring), as the surface has a more similar albedo throughout the fjord in summer. Open water surrounded by sea ice (in spring) further promotes local heat fluxes to the atmosphere (Ding et al. 2020). The absence of temperature differences generated by the distinguished conditions over ice-covered and ice-free areas in summer could explain the relatively homogeneous spatial structure in the second row in Figure 9. Thereafter, the spring measurements were made while cold melt water entered Billefjorden from the glacier Nordenskiöldbreen, as well as the snow-covered land around Billefjorden. This could cause a temperature gradient to develop, as a result of smaller sensible heat fluxes to the atmosphere in Billefjorden, compared to the fluxes over the relatively warm water further southwest in Isfjorden. The total dimension of melt water runoff decreases over the summer, following the lack of available snow on land (Pelt et al. 2012). The magnitude of runoff specifically from glaciers is controlled by temperature and precipitation conditions, which are most favorable in late spring and early summer. Based on this, one could argue that the melt water from glaciers does not on its own force a temperature gradient along Isfjorden's axis (as the difference is relatively weak in summer, around 1°C at its highest), but might contribute to the relatively cold areas close to the glaciers in several side fjords during the runoff peak periods.

As the gradient signal strength varies with the wind direction, it should be considered a relevant forcing for the gradient development. While the temperature difference along the fjord is around 3.5°C for NW and N winds in spring, the magnitude is closer to 1.5°C during

E winds, and around 0°C during SW winds in the same season. Additionally, although the gradient along the fjord is relatively weak in summer, the area closest to Nordenskiöldbreen is still around 2°C colder than the reference when the wind comes from the N and NW. This indicates that the colder areas in Billefjorden are specifically related to cold air from over the glacier moving down over the northeastern part of Isfjorden. As the snow on land melts in spring and early summer, the temperature difference between the air over land and water decreases, and in the summer months temperatures over land can be higher than over water (due to the high heat capacity of water) (Skogseth et al. 2020). When the incoming shortwave radiation gets limited again in autumn, and the land surface cools down below the water surface temperature, stronger temperature gradients (than in summer) occur. The seasonal difference in the gradient extent could therefore indicate that the contribution of advection is especially important for the times when the land surface temperature is lower than the sea surface temperature (as energy from the air is then not only extracted over Nordenskiöldbreen but also over land, before the drainage down to Billefjorden).

During W winds, in summer and autumn, the temperature gradient vanishes. The W wind plots show an opposite tendency in relation to the reference for summer and autumn, with overall negative anomalies in summer and overall positive anomalies in autumn. As the temperature anomaly distribution in both cases looks homogeneous, indicating an air mass with similar thermal characteristics in the horizontal dimension, one could assume that the W winds entails an inflow of air from over the open ocean in the west that reaches more or less all the way up to the northeastern-most parts of the fjord, while this is not the case for other wind directions. Yet, a warmer area prevails in the southwestern part of Isfjorden for (more or less) all wind directions in spring and autumn, indicating an interaction between the relatively warmer marine air and the air inside the mouth of Isfjorden (Skogseth et al. 2020). The opposing tendencies during summer and autumn during W winds could possibly be explained by land fetch impacting the reference data, as measurements from LYR are used during W winds, and there is around 1 km of land in between the airport and the coast on its western side. It is worth noting that the plot of W winds in autumn contains considerably fewer measurements than the plot of W winds in summer (see Figure 14 in Appendix A).

During NE and E winds, Figure 9 shows an area around the mouth of Sassenfjorden with cold temperatures relative to the rest of the fjord, during all seasons. The signal is the strongest, around 2°C colder than the rest of the fjord, for E winds during summer. The cold area around Sassenfjorden coincide with peaks in wind speed for the same area and wind directions (see Figure 12), and can therefore be assumed to be linked to channeling effects, discussed in detail in Section 4.2. In addition to the thermal impact of the underneath surface from which the air mass origins (advected characteristics), higher wind speeds affect the remaining factors for temperature change mentioned in Equation 3. The contributions to temperature change from conduction, radiation and turbulent fluxes are all controlled by interactions between the air mass and the underlying surface. Even though the turbulent surface heat fluxes are amplified by high wind speeds close to the surface, the movement of the air limits the possibility for the air to reach thermal equilibrium with the surface. During high wind speeds, the air mass does not stay long enough for the surface to heat it according

to its full capacity, which could explain the colder area around the mouth of Sassenfjorden during the wind channeling phenomena.

Figure 9 further shows a temperature gradient across the width of Isfjorden, especially apparent during NE and E winds in the summer, with temprature differences of approximately 2°C. The gradient occurs between the (warmer) southeastern side of the fjord, around the area of Adventfjorden and further out along the coast of Isfjorden, and the (colder) northwestern side around the area of Ymerbukta. The signal could be forced by relatively high SST along the southern shorelines, as warm inflow of Atlantic water from the WSC follows the southern shoreline of Isfjorden, while the cold freshwater outflow from the fjord's inner parts instead follows to the northern shoreline (Skogseth et al. 2020). In summer, the cold area at the northwestern side could possibly be connected to the channeling effects mentioned in previous paragraph. It is also reasonable to assume that the relatively warm area on the southeastern side is an indication of land fetch, as the signal is comparably strong during the summer, when we can expect the air from over land being warmer than the air from over water (Skogseth et al. 2020).

As mentioned in Section 2.3.1, inversions play an important role in the atmospheric temperature conditions in Arctic regions. Though these are commonly connected to radiative cooling of land during the polar night (outside of the measurement period for this thesis), advective processes (cold air close to the surface due to katabatic flows and warm air higher up in the atmosphere) have been found to greatly impact the occurences of summer inversions (Vihma et al. 2011). As measurements at BHN are conducted at a height of around 4 meters (closer to the surface than measurements in the mobile network, conducted at around 17 m) a case of inversion could be present in the data set as relatively higher temperatures from the mobile network compared to the reference. The height difference in itself theoretically introduces a temperature difference of ($\pm$, sign depending on what reference station is used as the measurements at LYR airport are conducted at 28 m) 0.1°C between the mobile and reference stations, following the dry-adiabatic lapse rate. Figure 9 shows that the 0.1°C difference is not large enough to disturb the apparent signals resulting from the remaining spatial differences. Katabatic flows close to the surface would be expected during northwesterly winds at the BHN station, which is accounted for as data is instead used from LYR airport during times of that prevailing wind direction. However, advection of warm air aloft is not accounted for, and could possibly result in an inversion showing up as higher temperature anomaly values. In contrast, unstable stratification of the atmosphere would show up in the data set as relatively colder temperatures from the mobile network compared to the reference. As instability is expected in summer, the relatively cold signal in the second row of Figure 9 could reasonably be connected to the height difference between BHN and the mobile network. The fact that no clear warm signal is present when the LYR airport is used could be explained by the vertical temperature gradient being stronger closer to the surface than between two heights higher up in the atmosphere.

For some of the binned categories in Figure 9, such as SE and E winds during spring, and W winds during autumn, the grid-boxes contain fewer than 10 data points, see Figure 14

in Appendix A. This makes the statistical analysis less robust than for the remaining categories, and it should therefore be considered that the results based on those subplots are more sensitive to potential outliers in the data sets.

Further, it could also be the case that the conditions measured at by the stationary AWS's at certain times were not representative as a reference of Isfjorden's meteorological conditions. Especially during W winds in autumn, the temperature distribution throughtout Isfjorden is notably homogeneous. Possible differences within the grid-boxes are naturally evened out as only averages are shown, but it is suspicious that no variability at all occurred in between the averaged data in the different grid-boxes. The homogeneity could be an indicator of a systematic measuring error or disturbance at the reference station, but more measurements during the same conditions would be needed for conclusions to be made.

4.1.2   Spatial Specific Humidity Distribution

In Figure 10, the spatial patterns of the specific humidity anomalies during different seasons and wind directions are shown. The amount of measurements in every grid-box is shown in Figure 14 in Appendix A. Similarly to the signal in Figure 9, an overall horizontal gradient from the mouth to the head of the fjord prevails for several seasons and wind directions. Although the strengths in the humidity gradient signal differ between the seasons, the overall specific humidity patterns are relatively similar for the same wind directions. In spring, the difference in specific humidity from mouth to head over the fjord's axis measures around 0.6 g/kg for N winds, and around 0.2-0.4 g/kg for NE and E winds. Data points are missing for the outer part of Isfjorden during SE and S winds, with a relatively homogeneous distribution of humidity in the inner part of the fjord. During W and NW winds, the horizontal variability over the fjord is close to 0 g/kg, though an area of higher specific humidity is visible around the southern coast during W winds. In summer, a difference of around 1 g/kg prevails during N winds. For NE-S winds in the same season, the humidity content is around 0.2-0.4 g/kg higher in the outermost part compared to the innermost part of the fjord. A homogeneous structure occurs during SW and W winds, but during NW winds the horizontal difference again reaches values around 1 g/kg. In autumn, the magnitude of the difference is about 0.6 g/kg for N-SE winds. For the remaining wind directions, the gradient is weaker; around 0.2 g/kg for SW and NW winds.
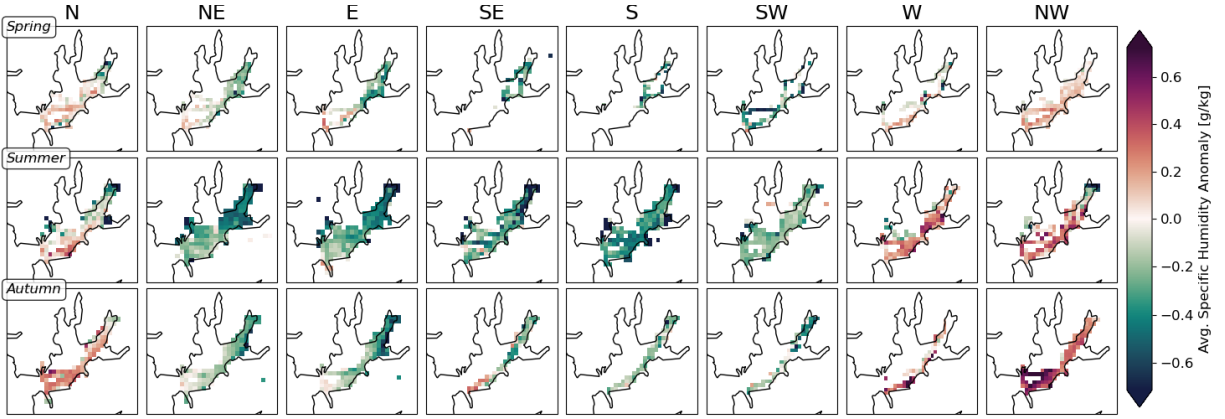
Figure 10: Spatial distribution of average specific humidity anomalies for different seasons (rows) and wind directions (columns).

Figure 10 shows the specific and not the relative humidity (see Section 2.1.2), but specific humidity can still be related to temperature. In spring and autumn in the Arctic region, relatively warm air can be an indicator of marine air advection (as the air is often warmer over the ocean than over land during those seasons). Marine advection entails the premise of relatively high (unlimited) available water for evaporation, compared to the air advected from over land. Moreover, specific humidity is determined by the water vapor pressure (see Equations 5 and 6), and as shown in Figure 1, the eligible number of water vapor pressure values (and consequently specific humidity) before saturation increases with temperature.

The strikingly low specific humidity area in the northern part of Isfjorden, during N winds and all seasons, can reasonably be related to the dry-air advection processes from over Nordenskiöldbreen mentioned in Section 4.1.1. A similar pattern is apparent for NE winds, but with smaller specific humidity differences along the fjord (than for N winds) in summer and autumn. Initially, when comparing the specific humidity gradient strength during N and NE winds, it appears that the NE wind direction is associated with drainage of air reaching further south in Isfjorden than during N wind directions (for all seasons), as the specific humidity distribution indicates an air mass with comparably homogeneous characteristics. Further, it is reasonable to expect mechanically forced winds out of Isfjorden during the NE direction, as it aligns with the orientation of the fjord's axis. However, the results in the E-SW columns show distributions similar to the NE column, rather indicating that the wind direction is only considerably important for the overall spatial humidity distribution when a shift occurs to westerly winds. The gradient signal could possibly indicate that the components of the NW wind entail an inflow from over the ocean and an outflow down Nordenskiöldbreen simultaneously.

Addition of cold fresh melt can be expected to impact the humidity distribution, as the runoff water is relatively cold compared to the water residing in the middle of the fjord, and more energy is needed to force an upward latent heat flux in those areas. As the specific humidity

gradient between the surface and the atmosphere determines the latent heat flux, the possible local differences in the flux magnitude increases with increased temperatures (described more in Section 4.1.3). Therefore, SST differences due to melt water runoff are only expected to be important for the spatial humidity variability during conditions when the fjord's water surface is comparably warm (enabling larger vertical gradient differences between the areas with residing fjord water and areas with melt water) and when the air temperature is horizontally homogeneous or comparably cold (for it not to dominate the impact on the specific humidity distribution). Figure 10 shows relatively low specific humidity areas in Trygghamna, Ymerbukta, Borebukta, Colesbukta, Adventfjorden, Sassenfjorden mouth and Billefjorden, during S winds in summer. Comparison with Figure 9 shows that the temperatue distribution across the fjord was relatively homogeneous during the same conditions, and that several of the low humidity areas do not coincide with relatively low temperature areas. The average temperature anomalies are only slightly lower (than the reference) in the bays along the northwestern fjord side and close to Nordenskiöldbreen in Billefjorden. The relatively clear patterns in the specific humidity data could possibly be explained by decreased latent heat fluxes due to the cold water input. However, the low humidity areas on the southeastern fjord side can not be closely related to glacial runoff water. Instead, the low specific humidity anomaly values at those areas likely indicate outflow from over dry (but not as cold as over the glaciers) land.

As mentioned in Section 2.3.2, humidity inversions have been found to be stronger over sea ice compared to open water, meaning that the humidity increase with height in the atmosphere was larger over sea ice. Similarly to the inversions discussed in Section 4.1.1, a case of humidity inversion could show up in the analyzed anomaly data set as a relatively high humidity content for the paths in Figure 10. As sea ice would only occur in Isfjorden during the spring months, this could possibly explain some of the humidity gradients along the fjord during the spring period. Conclusions regarding this would require establishment that sea ice was prevailing around the BHN station and close to the position of the mobile measurements simultaneously, further studies could advantageously be conducted about the possible impact of this process on the humidity measurements.

4.1.3 Temperature and Humidity Synergy

Figure 11 shows how the difference in temperature between the sea surface and atmosphere varies over the measuring period, as well as the strength of the horizontal gradients in temperature and humidity across Isfjorden (discussed in Sections 4.1.1 and 4.1.2). The difference in SST and air temperature is positive in spring, with a peak of around 10°C difference in late April, but decreases down to approximately -1°C in the beginning of June. For the following months, the difference remains negative but is close to 0°C until the beginning of August, where it measures -2.5°C. Further, panel b) in Figure 11 shows negative temperature gradients (weekly average over areas shown in Figure 8) for the measuring period until the beginning of June. The gradient magnitude differs over spring, with the highest absolute difference of around 2°C in the first week of May. During the summer months, the gradient is on average positive for the majority of the weeks, with differences of approximately 0.5°C. From the first week of August, the average temperature anomalies are relatively similar between

the inner and outer part of the fjord, with differences between -0.5 and 0.5°C. The second row in panel b) shows that the specific humidity gradient on weekly average is negative for the majority of the measuring period, with the exception of the period when the shift between June and July happened. During that week, the average difference between the inner and outer part of the fjord was approximately 0.1 g/kg. Two weeks later, the gradient was positive but only reached a value of around 0.05 g/kg. The peaks in (averaged) absolute specific humidity difference between the inner and other parts of the fjord took place in mid-April and late May, where the difference measured around -0.4 g/kg.
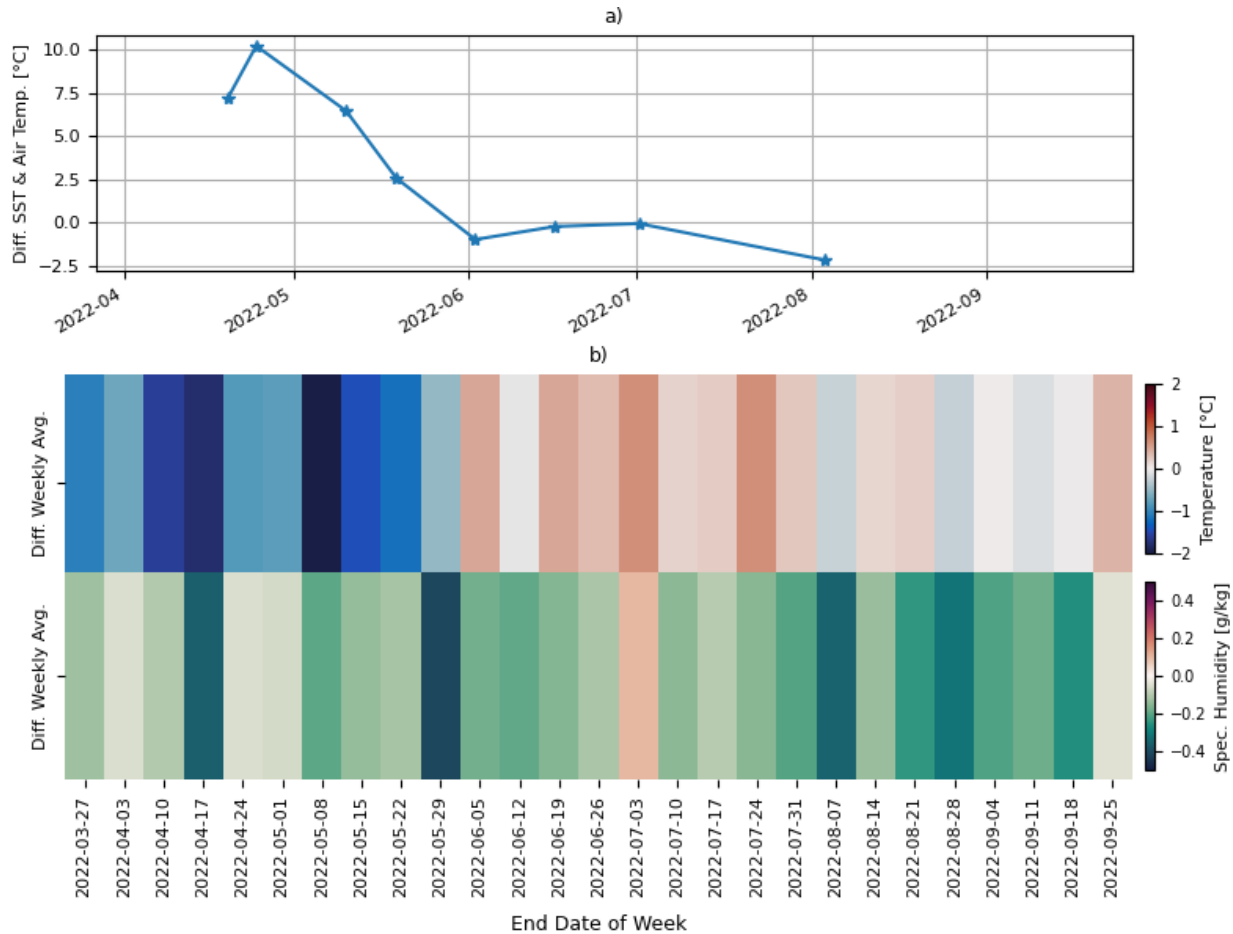
Figure 11: a) the difference between SST (sample values from IsA, see Section 3.3.3) and ambient air temperature from the stationary network from mid-April to late September 2022. Positive values indicate higher SST than air temperature. b) weekly average difference (in temperature and specific humidity anomalies) between the inner and outer part of Isfjorden. The limits of the "inner" and "outer" regions of the fjord were based on the spatial resolution necessary to resolve the gradient signals seen in Figures 9 and 10. Negative values represent average negative gradients directed from the mouth to the head of Isfjorden (meaning that the values are higher at the outer part than at the inner part of the fjord). Positive values imply positive gradients from the mouth to the head of Isfjorden (values are higher at the inner part than at the outer part of the fjord).

Based on the time series in Figure 11, it is reasonable to conclude that the shift from negative to positive weekly average temperature gradients in early June is connected to the shift to negative SST and air temperature differences. The variation of the temperature gradient over time (in relation to the SST and air temperature difference) indicates that the temperature of the air residing internally in Billefjorden is primarily influenced by advection processes from over land, while the interaction with marine air masses dominates the impact on the air residing in the outer part of the fjord, over the months.

It is additionally worth noting the apparent lack of connection between the air temperature and specific humidity gradient distributions. Instead of following a tendency similar to the temperature gradients', the absolute magnitude of the weekly averaged specific humidity gradient is generally increasing over the months (with the some exceptions). As the surface latent heat flux is determined by the specific humidity gradient between the surface and the atmosphere, which depends on temperature, it would be intuitive to expect that greater spatial variability (stronger gradient) in temperature would result in higher specific humidity variability (stronger gradient). However, as shown in Figure 1, the differences between water vapor pressure values are relatively small during cold temperatures, which reduces the importance of local air temperature differences (for spatial variability due to latent heat flux variability). Hence, the increased absolute specific humidity gradient values from spring to summer can be explained by relatively cold air temperatures in spring (compared to summer) limiting the possible magnitude of latent heat flux differences.

The temperature dependency of the specific humidity variable can, in other words, not solely explain the spatial humidity distribution. Even when the gradient signal in Figure 11 is reversed for the temperature data, a negative specific humidity gradient directed from the mouth to the head of Isfjorden occurs. The specific humidity content is thus, on weekly average, higher at the outer parts of the fjord compared to the inner for all weeks throughout the measuring period (except one, which can be percieved as an outlier). The overall high specific humidity in the outer part (compared to the inner part) of Isfjorden implies that the most important impacting factor for the spatial specific humidity variability over the fjord is advection from surfaces with differing available water content.

4.2   Wind Speed Patterns

In Figure 12, wind speed anomalies are binned into categories of ambient wind speed value thresholds and wind directions. Figure 15 in Appendix A shows the number of data points in every grid-box. Overall, Figure 12 shows that the wind field over the fjord gets more heterogeneous as the ambient wind speed increases, which for instance can be seen in the N winds columns. Further, a signal of relatively high wind speed around the Sassenfjorden mouth is apparent for ambient wind speeds of 6.4-9.6 m/s and 3.2-6.4 m/s during N winds, while the pattern is visible in all rows in the NE and E columns. For SE winds, the distribution is comparable to that of N winds, with the peak around Sassenfjorden mouth only showing for ambient wind speeds higher than 6.4-9.6 m/s. Tendencies of a sheltered area along Isfjorden's southeastern coast occur for wind speed threshold values higher than 3.2 m/s during SE winds and for threshold values higher than 6.4 m/s for S winds. The sheltered area along the southeastern Isfjorden coast, as well as in the outer part of Billefjorden, is clear for all cases in the SW column. The wind speed distribution over the fjord is similar regarding shelter during SW and W winds, in addition to the earlier mentioned signal of relatively high wind speeds around Sassenfjorden and Tempelfjorden again occurring for W winds. During NW winds, earlier mentioned sheltered areas appear for 6.4-9.6 m/s and 3.2-6.4 m/s, while the distribution is overall homogeneous for 0-3.2 m/s ambient wind speed.

For the 3.2-6.4 m/s row in the N column, the measurements from the area around Sassenfjorden mouth reach approximately twice the value (and the rest of the fjord around 140%) of the reference wind speed values. During ambient wind speeds between 6.4-9.6 m/s, the magnitude of the wind speeds anomalies are generally lower, while the difference in percentage units between the Sassenfjorden area and the rest of the fjord is similar in between the W-SE winds (with a peak of around 120% of the reference value around the Sassenfjorden area). For the 9.6-12.8 m/s row during NE and E winds, the wind speed magnitude is around 40% of the reference station for all parts of the fjord except the area around the mouth of Sassenfjorden, where the wind speed value is more or less equal to BHN. For W winds, wind speeds of twice the values compared to the reference prevails in Sassenfjorden and Tempelfjorden, during ambient winds of 3.2-6.4 m/s and 0-3.2 m/s. The Sassenfjorden signal is visible (although weaker than for the remaining rows) in the lowest ambient wind speed range row during NE, E and W winds, while the distribution is consistently around twice the reference value for the rest of the columns during the same ambient wind speed conditions.

A pattern of a sheltered area along Isfjorden's southeastern coast generally occurs in Figure 12 during SW-N as well as SE wind directions. In the area, wind speed values are consistently around 60%-80% of the reference values across the wind directions during 6.4-9.6 m/s, with the exception of N and SW winds where the wind speed is approximately 90% (of the reference). For ambient wind speeds of 3.2-6.4 m/s, the measured wind speeds in the area are approximately the same as those at the reference station for all mentioned wind directions. During southerly winds for 6.4-9.6 m/s ambient winds, the wind speed in Billefjorden (especially its southeastern side) is around 80%-90% of the reference, while the wind speeds throughout the remaining parts of the fjord range between approximately 140%-180% of the reference. For S winds, the wind speed conditions are consistently around twice the value of the reference station, except for the sheltered areas apparent during ambient wind speeds of 6.4-9.6 m/s.
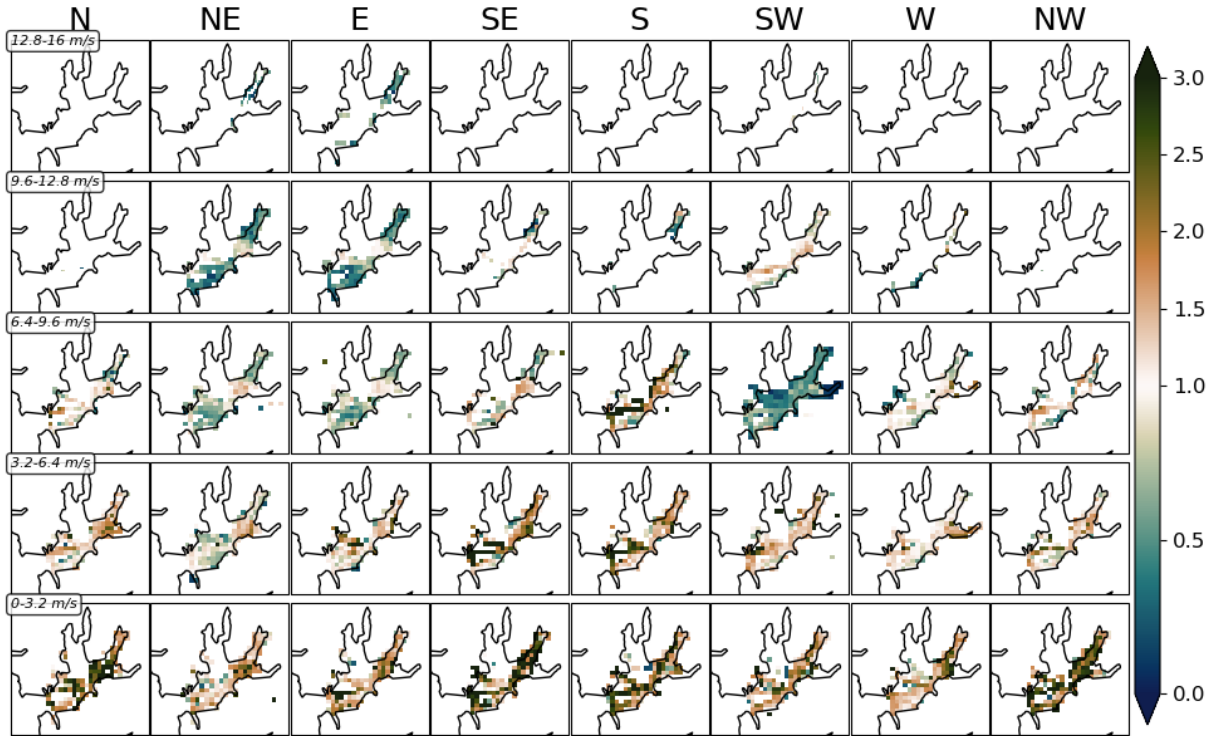
Figure 12: Spatial distributions of average wind speed anomalies in March for certain wind directions and ambient wind speed thresholds. The wind speed threshold bins correspond to 0-3.2 m/s, 3.2-6.4 m/s, 6.4-9.6 m/s, 9.6-12.8 m/s, and 12.8-16 m/s of the 99% qualite of ambient wind speed over the entire measuring period.

As mentioned in previous paragraphs, one striking pattern shown in Figure 12 is relatively high wind speeds around the mouth of Sassenfjorden during NE and E winds. The pattern is especially clear when the ambient wind aligns with the orientation of the fjord, which indicates that the wind speed maximum can be related to a mechanically forced channeling of the local wind out of Sassenfjorden. The obstruction of the mountain sides limiting the mass' extent (resulting in increased velocity), and the comparably low friction from the water surface in the fjords, direct the air masses to follow the fjord's axis and enables acceleration as they move along the path. This was expected for E wind directions (the rough orientation of Sassenfjorden), but the data shows a specifically clear signal during NE winds, and also to some extent during N winds. This is possibly indicating that the conditions are especially favorable for the air mass to accelerate when the channeling effect prevails also in Tempelfjorden (the northeastern directed fjord "behind" Sassenfjorden). Although the angle between the fjords is quite sharp, the opening of Sassendalen in combination with the widening of the fjord valley redirects the wind into Isfjorden during NE winds. A similar pattern can also be seen during westerly winds, further implying that the results for W winds are mechanically forced channeled flow, but into Sassenfjorden instead. The results for W winds during 3.2-6.4 m/s shows a relatively high local wind speed all the way into Tempelfjorden, which is another

indication of the effective redirection of the flow between Sassenfjorden and Tempelfjorden. However, it is worth noting that no cold area can be connected to the high wind speed area for W winds, while this is the case for N and NE winds (see Figure 9). The differences in temperature anomaly patterns for the channeled flow imply that the impact of advection of cold glacial outflow is more important (for the temperature distribution) than the limitation of air and surface reaching a state of equilibrium due to the wind's rapid movement. As BHN is situated along the axis of the Sassenfjorden inflow and outflow, the wind speeds at the reference station for these cases can also be assumed to be impacted by the channeling effects. This might be an explanation of the notably low wind speeds further south and north into the fjord (in relation to BHN) during NE and E wind directions. The low signal is less clear for the W wind sector, which could possibly be related to the fact that the LYR airport stations is not affected by the channeling effects in the same way.

Reoccurring areas of relatively high wind speeds mid-fjord, close to the Isfjorden mouth, and relatively low wind speeds closer to the southeastern coast at the outer part of the fjord can also be seen in Figure 12. The higher wind speed area around the Isfjorden mouth, for example seen during SW, W and NW winds, possibly implies an inflow to the fjord that is eventually slowed down due to impact of surrounding obstructions (the fjord valley sides). During S winds, the wind speed is comparably high throughout the fjord, with exception of the innermost parts. The relatively sheltered conditions in Billefjorden could be a result of mechanical turbulence effects, caused by the obstructions around its mouth, being greater with higher wind speeds. As mentioned in Section 1, Kilpeläinen et al. (2011) showed that incoming air is not effectively transported into the side valleys of Isfjorden. With turbulent eddies occurring around the narrow opening, the air flow might get deflected instead of entering Billefjorden. The same reasoning could be an explanation of the signal being more clear when the air moves in a western direction (which is not favorably aligned for an inflow into Billefjorden and therefore would result in more turbulence around the Billefjorden mouth), compared to cases were the flow is more aligned with the Billefjorden axis.

The spatial variability over Isfjorden is comparably weak during low wind speeds, with relatively homogeneous conditions during the majority of the wind directions for ambient wind speeds lower than 3.2 m/s, see Figure 12. The variability increases with increased wind speeds for all wind direction but S winds, where the wind speed is more or less constantly around twice the value of the wind speed at the reference station, throughout the entire fjord. Figure 15 in Appendix A shows an eligible number of data points during S winds, which decreases the risk of low variability appearing solely as a consequence of sparse amounts of measurements. As the plot shows the local wind speeds in relation to the wind speed at BHN, one possible explanation of the homogeneous distribution could be the height difference between the mobile network and the BHN station. As wind speed generally increases with height, the disturbance could be expected during multiple wind direction conditions in the data set, but it is still reasonable to assume that local factors may result in especially high turbulence near the surface at reference station during S winds.

In Sections 4.1.1 and 4.1.2, the meteorological quantities were discussed in regards to inflow

from the ocean during W winds. Figure 14 in Appendix A shows that the majority of the data during W winds were recorded during the summer months. For SW and W winds, the wind speed along the fjord's axis is relatively homogeneous (compared to the distribution during other prevailing wind directions, and with the exception of the area around Sassenfjorden), which further concludes the earlier discussed inflow to Isfjorden from over the ocean.

5 Method Assessment

In the following section, a number of possible sources of uncertainties due to chosen methods are discussed and assessed. Section 5.1 covers possible uncertainties in the results due to the interpolation and weighting processes, the influence of chosen grid-box extent is assessed in Section 5.2, and uncertainties related to the placements of the instrumentation are discussed in Section 5.3.

5.1 Interpolation and Weighting

As explained in Section 3.3.1, data from LYR airport was used as reference for the anomaly calculations during times with prevailing northwesterly winds. As the LYR airport data set only has an hourly temporal resolution, it was resampled onto a 1-min grid using linear interpolation in order to match measurements from BHN and the mobile network (as covered in Section 3.3.2). This up-sampling introduces errors, as the variation in the meteorological variables are "smoothed" and momentary changes due to rapid processes are lost. Regarding temperature and relative humidity, values from LYR airport are instantaneous values, while the wind speed values are averages measured over the 10 minutes before logging. For the wind speed, where the scale of the impacting processes can be small, the interpolation can be assumed to reduce the variability that likely would have shown using higher resolution measurements. It is not possible to say how the anomaly values were impacted by the interpolation, as the true ambient wind speed values could have been both higher and lower compared to the mobile wind speed value for the same time. The same reasoning can be applied regarding the change in ambient temperature and humidity, although the effects are expected to have a stronger influence on the wind than on the remaining variables. In any case, the interpolated LYR airport data set can be considered to show the correct ambient change in the studied meteorological parameters.

During W and N winds, the stationary data set consists of values that combines the conditions at two different parts of Isfjorden at the same point in time, which could entail disturbance in the data. As both BHN and LYR were chosen as reference due to their favorable positions, and complementing abilities to measure the atmospheric conditions over the fjord, the combination of the stations' measurements can be justified. It is, however, worth mentioning that the results of this study show reoccurring variation in all meteorological variables across the width of Isfjorden due to spatial factors. A coefficient of determination of magnitude 0.93 was obtained when studying the connection between the temperature measurements at the respective stations, see Figure 16 in Appendix A. It is also apparent in Figure 16 that the deviations from the regression model are larger during colder temperatures than during warmer, which could be interpreted as an implication of (relatively) similar measurements at the two stations during the warmer part of the year. For future research projects, it would be advantageous to setup the same type of station found at BHN on the opposite side of Isfjorden (in relation to BHN), close to the coast. In addition to the expected improvement of measurements during NW winds, it would also reduce the possible discrepancies between the data sets due to differences in measuring methods and instruments.

5.2 Extent of Grid-Boxes

As the data in Figures 9, 10 and 12 is presented as averages over spatial grid-boxes, the amount of data in every grid-box impacts the resulting anomaly values. Testing with different grid-box sizes showed different strengths in the signals discussed in Sections 4.1.1, 4.1.2 and 4.2. In order to ensure that the visualized patterns in the meteorological variables were meaningful, while still allowing a high spatial resolution, a grid of 50 boxes in every direction (corresponding to 1×1 km) was applied. As a lower limit was also set to eliminate all grid-boxes containing less than five data points. The amount of data in the grid-boxes varies, see Figures 14 and 15 in Appendix A, which displays a true overview of the occurrence of prevailing meteorological conditions. The certainty of the connection between the presented dimensions (such as the wind direction and temperature distribution during a certain season in Figure 9) increases with increased amount of available data. Ideally, measurements would be conducted using the same instrumentation, stationary and mobile setup over multiple years. Even though the data count for the different categories would continue to naturally vary, the expanded measuring period would result in less impact of the potential outliers in the data sets. Out of the signals shown in this study, the temperature and specific humidity gradients along and across the fjord, the temperature drop and wind speed peak around the Sassenfjorden mouth, and the increased homogeneity during marine inflow, could probably be resolved with larger grid-box sizes than what was used. Other patterns, such as those indicating channeling and advection from over glaciers in the relatively smaller side valleys, would probably not be resolved with lower resolutions. For a more detailed investigation, all measurements (not averages) from within certain grid-boxes of interest could be compared, with the extent of the grid-boxes being adapted to the spatial extent of the signals found in this study. The analyses of the patterns would also be strengthened with added information from the northwestern and easternmost parts of Isfjorden, though that data supply is limited by the paths that the ships follow.

5.3 Placement of Instrumentation

The results in this thesis are further influenced by the methods used (and choices made) when setting up the instrumentation. For the stationary network, some disturbances (due to land fetch) introduced by the location of the BHN station in the terrain are discussed in Section 3.2.3 and was accounted for in this thesis. However, it is not possible to exclude the risk of the BHN station measurement data being impacted by local factors that have not been identified in this study, as the wind speed measurements during southerly winds could possibly imply (discussed in Section 4.2). Such local factors could e.g. be obstructions related to the barrier between water and land, forcing turbulence and flow distortion, resulting in measurements of processes apart from the overall flow prevailing over Isfjorden. In order to minimize the disturbances on the reference network, several stations at multiple locations along the coast of Isfjorden could be combined, so that data is only used from each station when the conditions are favorable for undisturbed flow. For this to be realistic, more near-surface measurement data from locations throughout the fjord and research focusing on identifying the impacting factors is needed.

Flow distortion is an issue regarding the mobile network as well. The AWS's positions at the highest possible point of each ship were chosen to limit the impact on the flow introduced by the shape of the ships. As MS Polargirl and MS Billefjord are both streamline shaped, they are built to direct the air flow along the sides of the ships and therefore to generally avoid the air getting deflected upwards when hitting the stern. MS Bard, however, instead has a flat stern acting as a wall when the air hits it. The portion of air hitting the ship, instead of going in between the keels, will create turbulence that is possibly propagated upwards to the location of the AWS. In order to find the best position for placing a weather station on MS Bard, data measured at different locations of the ship could be compared with measurements conducted at the other ships for the same time period. The ships would have to follow the exact same route for the measurements to be directly comparable, which is not realistic, but measurements from different locations on MS Bard would enable a quantitative analysis of the perturbation (from the other ship data) differences between different AWS locations on MS Bard.

The wind measurements performed by the mobile AWS's could further be exposed to disturbances due to the ships tilting. It is reasonable to assume that the tourist cruises would be cancelled during times of extreme risk for tilting, but even during relatively low wave conditions, the AWS's will be influenced to some extent. The importance of tilting for uncertainties is not considered predominant during the results in this thesis, as the wind direction measurements from the mobile network are not studied per se. It is still worth noting that errors could have been introduced during the calculation of the wind speed data sets, as corrections for the ships movement are based on the measured wind direction (see Section 3.2.1). The impact of tilting in the data could be reduced by averaging the wind direction components separately over short time spans, to reduce the impact of the vessel leaning in different directions. This could, however, introduce other uncertainties in the data set, as the wind direction can suddenly change substantially and an average between different wind directions then is not meaningful.

The height difference between the reference and mobile data sets impacts the meteorological variable anomalies, as mentioned in Section 4. Signals in the data can be interpreted as processes explained by the height difference, but to support the analysis of the vertical atmospheric structure it would be advantageous to install additional weather stations at the locations of the reference stations at the same height as the mobile network or correct the measurements using a standard wind profile (based on e.g. the logarithmic wind law and Monin-Obukhov similarity theories).

6 Conclusions

This study was performed to identify and quantify the spatial variability in temperature, specific humidity, and wind speed over Isfjorden, Svalbard, and connect the variability to local and synoptic-scale conditions. This was done by analyzing data from a mobile weather station network, performing measurements throughout the fjord, in comparison with a stationary network measuring the large-scale variation in the meteorological variables. Conclusions based on the analyses follows:

A re-occurring temperature gradient along the axis of Isfjorden prevails, reaching a maximum value of 3.5°C from the head (colder) to the mouth (warmer) during the study period. The temperature gradient is strongest in spring (maximum recorded during N winds) and the direction of the gradient is shifted in summer due to the shifting relative measures of SST and air temperature. The gradient is connected to the impact of advected marine air and water inflow (synoptic-scale processes) close to the mouth, and to drainage winds (local-scale process) down the Nordenskiöldbreen glacier terminating in the area of the Isfjorden head.

A temperature gradient also occurs across the width of Isfjorden, from the northwestern (colder) to the southeastern (warmer) shorelines. The maximum temperature difference during the period was 2°C, which appeared for easterly winds in summer. The gradient is connected to air advection from over land (synoptic-scale) on the southeastern side and (local) cold runoff water from melting glacial ice on the northwestern side.

The humidity content of the air is consistently higher closer to the Isfjorden mouth than further into the fjord, with a maximum difference of 0.6 g/kg for N winds in summer (for the study period). This gradient prevails along Isfjorden throughout the study period. It is amplified by local advection through drainage winds internally in Isfjorden, but the main impact factor is differences in available water between the mouth and the areas surrounding the head of the fjord.

An area by the mouth of Sassenfjorden is systematically colder than the rest of the fjord, with a maximum temperature difference of around 2°C for E winds in summer. Analysis of the wind speed anomalies showed wind speeds around 140% (of the reference) in the same area for easterly winds. The pattern is connected to local advection, through forced channeling depending on the synoptic-wind situation, of air from glacial-covered land to the fjord.

Relatively high wind speeds prevail in the Sassenfjorden mouth region during westerly winds as well, with peak wind speeds around 200% (of the reference) during synoptic-scale winds of 0-6.4 m/s. Similarly to the peak during easterly winds, this is explained by forced channeling of the synoptic-scale wind.

The spatial variability in wind speed over Isfjorden is dependent on the synoptic-scale wind direction. For wind directions along the fjord's axis, the variability is relatively homogeneous. This is explained by the orientation of the fjord allowing an inflow of the mean wind.

7 Outlook

The work on this thesis has lead to a number of open questions, of which the most important ones shall be presented in the following.

Firstly, the technical and practical aspects of the weather station networks could advantageously be evaluated. To reduce impact on the results from measurement errors, quality control of the stationary network, e.g. through comparison with manual wind measurements for different ambient wind directions, would be beneficial. By identifying possible error sources, the network could be expanded and measurements combined to eliminate local impact factors and improve the quality of the reference data set. The same holds for the mobile data set, where improvement could be provided by further studies on methods for accounting for flow distortion on the specific ships. To minimize possible influence from sources such as heating from the ship's surface or near-by electronics, the location of the instrumentation could be tested and evaluated (by comparison with data conducted on a ship as close to the ideal case for measurements as possible, naturally). In addition, it would be beneficial to expand the mobile network further to cover a larger part of the fjord.

Another valuable addition, for supporting the conclusions on advection in this study, would be to relate the found occasions of local advection to surface cover. Initially, measurements from the fjord could be studied together with measurements from land. Foundation could be provided by comparing a time series from e.g. Nordenskiöldbreen or Colesbukta, with a time series from the mobile network from that area during the same time. The indications could be supported further by monitoring the change in surrounding surface covers. Thus, the origins of locally advected heat and humidity could be studied along with melting, thawing and drying processes on land surrounding the fjord. The understanding would also be benefited by a similar analysis (as in this thesis) of meteorological patterns including data of sea ice extent. Connections between local surface cover and the three major meteorological variables could possibily be found, if data from e.g. sea ice charts or satellite images was used in the analysis.

References

Argentini, A. Pietro Viola, G. Mastrantonio, A. Maurizi, T. Georgiadis & M. Nardino (2003), 'Characteristics of the boundary layerat Ny-Ålesund in the Arctic during the ARTIST field experiment', *Annals of Geophysics* **46**(2).

BrimExplorer (n.d.), 'Svalbard boat tours'.
URL: *https://brimexplorer.com/destination/svalbard*

Chen, S. & Wu, R. (2018), 'Impacts of early autumn Arctic sea ice concentration on subsequent spring Eurasian surface air temperature variations', *Climate Dynamics* **51**(7-8), 2523–2542.

Dahlke, S., Hughes, N. E., Wagner, P. M., Gerland, S., Wawrzyniak, T., Ivanov, B. & Maturilli, M. (2020), 'The observed recent surface air temperature development across Svalbard and concurring footprints in local sea ice cover', *International Journal of Climatology* **40**(12), 5246–5265.

Dai, A., Luo, D., Song, M. & Liu, J. (2019), 'Arctic amplification is caused by sea-ice loss under increasing CO2', *Nature Communications* **10**(1), 121. Number: 1 Publisher: Nature Publishing Group.

Deng, J. & Dai, A. (2022), 'Sea ice–air interactions amplify multidecadal variability in the North Atlantic and Arctic region', *Nature Communications* **13**(1), 2100.

Ding, Y., Cheng, X., Li, X., Shokr, M., Yuan, J., Yang, Q. & Hui, F. (2020), 'Specific Relationship between the Surface Air Temperature and the Area of the Terra Nova Bay Polynya, Antarctica', *Advances in Atmospheric Sciences* **37**(5), 532–544. Company: Springer Distributor: Springer Institution: Springer Label: Springer Number: 5 Publisher: Science Press.

Esau, I. & Repina, I. (2012), 'Wind Climate in Kongsfjorden, Svalbard, and Attribution of Leading Wind Driving Mechanisms through Turbulence-Resolving Simulations', *Advances in Meteorology* **2012**, e568454. Publisher: Hindawi.

Eugster, W., Rouse, W. R., Pielke Sr, R. A., Mcfadden, J. P., Baldocchi, D. D., Kittel, T. G. F., Chapin III, F. S., Liston, G. E., Vidale, P. L., Vaganov, E. & Chambers, S. (2000), 'Land–atmosphere energy exchange in Arctic tundra and boreal forest: available data and feedbacks to climate', *Global Change Biology* **6**(S1), 84–115.

Francis, J. A. & Vavrus, S. J. (2012), 'Evidence linking Arctic amplification to extreme weather in mid-latitudes', *Geophysical Research Letters* **39**(6).

Göckede, M., Kittler, F., Kwon, M. J., Kwon, M. J., Burjack, I., Heimann, M., Heimann, M., Kolle, O., Zimov, N. & Zimov, S. (2017), 'Shifted energy fluxes, increased Bowen ratios, and reduced thaw depths linked with drainage-induced changes in permafrost ecosystem structure', *The Cryosphere* **11**, 2975–2996. Publisher: Copernicus Publications.

Haiden, T., Janousek, M., Vitart, F., Ben-Bouallegue, Z., Ferranti, L. & Prates, F. (2021), 'Evaluation of ECMWF forecasts, including the 2021 upgrade'. Publisher: ECMWF.

IPCC (2021), 'Climate Change 2021: The Physical Science Basis. Contribution of Working Group 1 to the Sixth Assessment Report of the Intergovernmental Panel on Climate Change. Chapter 7: The Earth's Energy Budget, Climate Feedbacks and Climate Sensitivity.', p. 132. **URL:** *https://www.ipcc.ch/report/ar6/wg1/*

Jocher, G., Karner, F., Ritter, C., Neuber, R., Dethloff, K., Obleitner, F., Reuder, J. & Foken, T. (2012), 'The Near-Surface Small-Scale Spatial and Temporal Variability of Sensible and Latent Heat Exchange in the Svalbard Region: A Case Study', *ISRN Meteorology* **2012**, 1–14.

Kazanskii, A. B. (2010), 'Katabatic glacier wind', *Doklady Earth Sciences* **434**(1), 1245–1248. Company: Springer Distributor: Springer Institution: Springer Label: Springer Number: 1 Publisher: SP MAIK Nauka/Interperiodica.

Kilpeläinen, T. & Sjöblom, A. (2010), 'Momentum and Sensible Heat Exchange in an Ice-Free Arctic Fjord', *Boundary-Layer Meteorology* **134**(1), 109–130.

Kilpeläinen, T., Vihma, T., Manninen, M., Sjöblom, A., Jakobson, E., Palo, T. & Maturilli, M. (2012), 'Modelling the vertical structure of the atmospheric boundary layer over Arctic fjords in Svalbard', *Quarterly Journal of the Royal Meteorological Society* **138**(668), 1867–1883.

Kilpeläinen, T., Vihma, T., Olafsson, H. & Karlsson, P. (2011), 'Modelling of spatial variability and topographic effects over Arctic fjords in Svalbard', *Tellus A: Dynamic Meteorology and Oceanography* **63**(2), 223–237.

Kitowska, M., Makuch, P., Petelski, T. & Piskozub, J. (2021), 'The influence of mesoscale land–sea breeze circulation on local wind climatology in the Svalbard fjords of Kongsfjorden and Hornsund', *International Journal of Climatology* **41**(S1), E832–E841.

Køltzow, M., Casati, B., Bazile, E., Haiden, T. & Valkonen, T. (2019), 'An NWP Model Intercomparison of Surface Weather Parameters in the European Arctic during the Year of Polar Prediction Special Observing Period Northern Hemisphere 1', *Weather and Forecasting* **34**(4), 959–983. Publisher: American Meteorological Society Section: Weather and Forecasting.

Lloyd, C. R., Harding, R. J., Friborg, T. & Aurela, M. (2001), 'Surface fluxes of heat and water vapour from sites in the European Arctic', *Theoretical and Applied Climatology* **70**(1), 19–33.

Met.no (n.d.), Norsk Klimaservicesenter, .
URL: *http://seklima.met.no/stations/*

Muckenhuber, S., Nilsen, F., Korosov, A. & Sandven, S. (2016), 'Sea ice cover in Isfjorden and Hornsund, Svalbard (2000–2014) from remote sensing data', *The Cryosphere* **10**(1), 149–158.

Nawri, N. & Harstveit, K. (2012), 'Variability of surface wind directions over Finnmark, Norway, and coupling to the larger-scale atmospheric circulation', *Theoretical and Applied Climatology* **107**(1), 15–33.

Nilsen, F., Cottier, F., Skogseth, R. & Mattsson, S. (2008), 'Fjord–shelf exchanges controlled by ice and brine production: The interannual variation of Atlantic Water in Isfjorden, Svalbard', *Continental Shelf Research* **28**(14), 1838–1853.

Nordeng, E., Brunet, G. & Caughey, J. (2007), Improvements of weather forecasts in polar regions, , WMO Bulletin.
URL: *https://public.wmo.int/en/bulletin/improvement-weather-forecasts-polar-regions*

Palo, T., Vihma, T., Jaagus, J. & Jakobson, E. (2017), 'Observations of temperature inversions over central Arctic sea ice in summer', *Quarterly Journal of the Royal Meteorological Society* **143**(708), 2741–2754.

Pelt, W. J. J. v., Oerlemans, J., Reijmer, C. H., Pohjola, V. A., Pettersson, R. & Angelen, J. H. v. (2012), 'Simulating melt, runoff and refreezing on Nordenskiöldbreen, Svalbard, using a coupled snow and energy balance model', *The Cryosphere* **6**(3), 641–659. Publisher: Copernicus Publications.

Polarcharter (n.d.), 'Us and our boats'.
URL: *https://www.polarcharter.no/us-and-our-boats*

Przybylak, R. (2016), *The Climate of the Arctic*, Vol. 52 of *Atmospheric and Oceanographic Sciences Library*, Springer International Publishing, Cham.

Przybylak, R., Araźny, A. & Ulandowska-Monarcha, P. (2018), 'The influence of atmospheric circulation on the spatial diversity of air temperature in the area of Forlandsundet (NW Spitsbergen) during 2010–2013', *International Journal of Climatology* **38**(1), 230–251.

Schalamon, F. (2022), Evaluation of the AROME Arctic Model Based on Mobile Observations in Isfjorden, Svalbard, Master thesis, Johannes Gutenberg University Mainz, University Center in Svalbard.

Serreze, M. C., Holland, M. M. & Stroeve, J. (2007), 'Perspectives on the Arctic's Shrinking Sea-Ice Cover', *Science* **315**(5818), 1533–1536. Publisher: American Association for the Advancement of Science.

Sjöblom, A. (2014), 'Turbulent fluxes of momentum and heat over land in the High-Arctic summer: the influence of observation techniques', *Polar Research* **33**(1), 21567.

Skogseth, R., Olivier, L., Nilsen, F., Falck, E., Fraser, N., Tverberg, V., Ledang, A., Vader, A., Jonassen, M., Søreide, J., Cottier, F., Berge, J., Ivanov, B. & Falk-Petersen, S. (2020), 'Variability and decadal trends in the Isfjorden (Svalbard) ocean climate and circulation – An indicator for climate change in the European Arctic', *Progress in Oceanography* **187**, 102394.

Sotiropoulou, G., Tjernström, M., Sedlar, J., Achtert, P., Brooks, B. J., Brooks, I. M., Persson, P. O. G., Prytherch, J., Salisbury, D. J., Shupe, M. D., Johnston, P. E. & Wolfe, D. (2016), 'Atmospheric Conditions during the Arctic Clouds in Summer Experiment (ACSE): Contrasting Open Water and Sea Ice Surfaces during Melt and Freeze-Up Seasons', *Journal of Climate* **29**(24), 8721–8744. Publisher: American Meteorological Society Section: Journal of Climate.

Stroeve, J. C., Serreze, M. C., Holland, M. M., Kay, J. E., Malanik, J. & Barrett, A. P. (2012), 'The Arctic's rapidly shrinking sea ice cover: a research synthesis', *Climatic Change* **110**(3), 1005–1027.

Stull, R. (2017), *Practical Meteorology: An Algebra-based Survey of Atmospheric Science*, 1.02b edn, University of British Columbia.

UNIS (n.d.), Isfjorden Adventfjorden Time Series (IsA), .
URL: *https://research.unis.no/isa/*

Vesselfinder (n.d.), 'BILLEFJORD, Passenger Ship - Details and current position - IMO 8415500 - VesselFinder'.
URL: *https://www.vesselfinder.com/vessels/BILLEFJORD-IMO-8415500-MMSI-231219000*

Vihma, T., Kilpeläinen, T., Manninen, M., Sjöblom, A., Jakobson, E., Palo, T., Jaagus, J. & Maturilli, M. (2011), 'Characteristics of Temperature and Humidity Inversions and Low-Level Jets over Svalbard Fjords in Spring', *Advances in Meteorology* **2011**, 1–14.

Vihma, T., Pirazzini, R., Fer, I., Renfrew, I. A., Sedlar, J., Tjernström, M., Lüpkes, C., Nygård, T., Notz, D., Weiss, J., Marsan, D., Cheng, B., Birnbaum, G., Gerland, S., Chechin, D. & Gascard, J. C. (2014), 'Advances in understanding and parameterization of small-scale physical processes in the marine Arctic climate system: a review', *Atmospheric Chemistry and Physics* **14**(17), 9403–9450.

Westermann, S., Langer, M. & Boike, J. (2011), 'Spatial and temporal variations of summer surface temperatures of high-arctic tundra on Svalbard — Implications for MODIS LST based permafrost monitoring', *Remote Sensing of Environment* **115**(3), 908–922.

Whiteman, C. D. & Doran, J. C. (1993), 'The Relationship between Overlying Synoptic-Scale Flows and Winds within a Valley', *Journal of Applied Meteorology and Climatology* **32**(11), 1669–1682. Publisher: American Meteorological Society Section: Journal of Applied Meteorology and Climatology.

Wickström, S., Jonassen, M. O., Cassano, J. J. & Vihma, T. (2020), 'Present Temperature, Precipitation, and Rain-on-Snow Climate in Svalbard', *Journal of Geophysical Research: Atmospheres* **125**(14).

WMO (2017), Navigating Weather, Water, Ice and Climate Information for Safe Polar Mobilities, Technical Report WWRP/PPP No. 5.
URL: *https://epic.awi.de/id/eprint/46211/1/012$_W$WRP$_P$PP$_N$o$_{52}$017$_1$1$_O$CT.pdf*
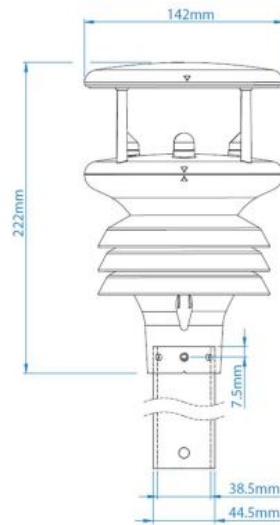
A   Appendix

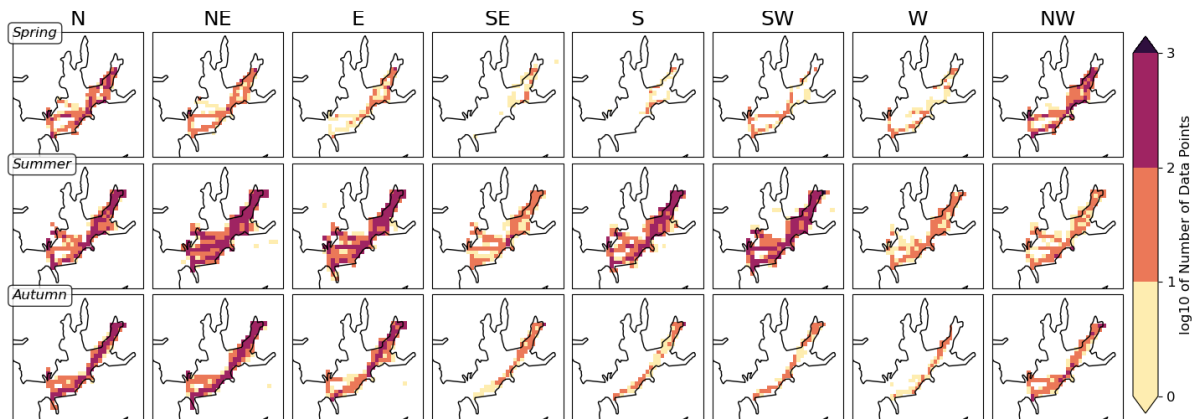Figure 13: Dimensions of MaxiMet GMX500 (*USER MANUAL For Compact Weather Stations*).

Figure 14: Number of data points in each bin for the season and wind direction data sorting
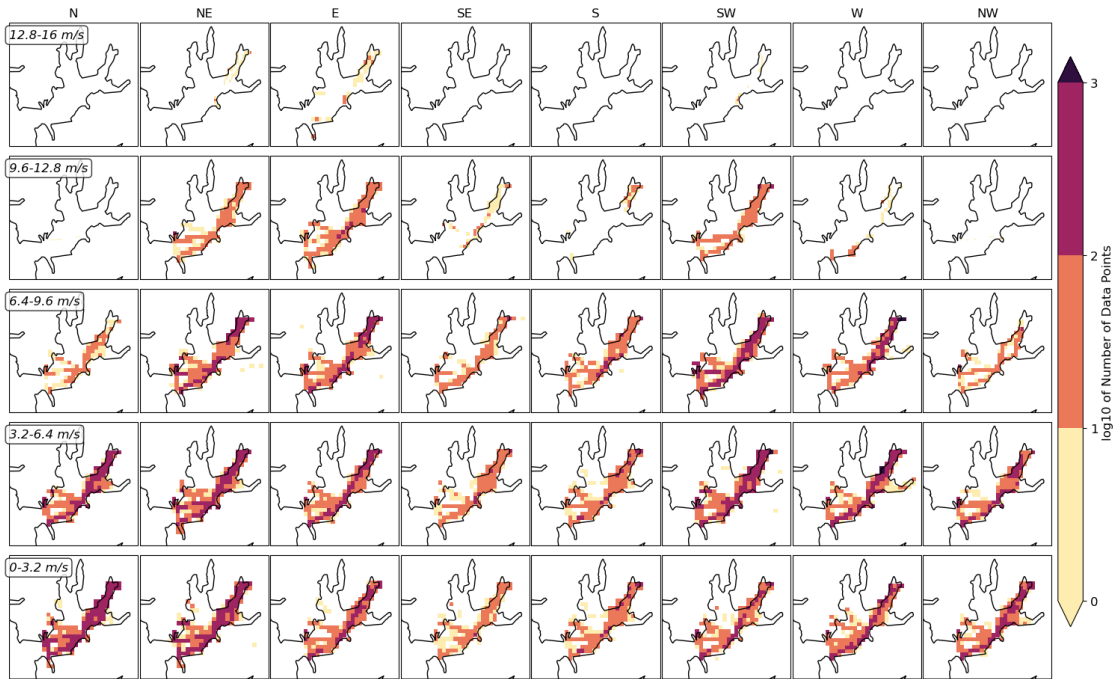
Figure 15: Number of data points in each bin for the wind speed and wind direction data sorting
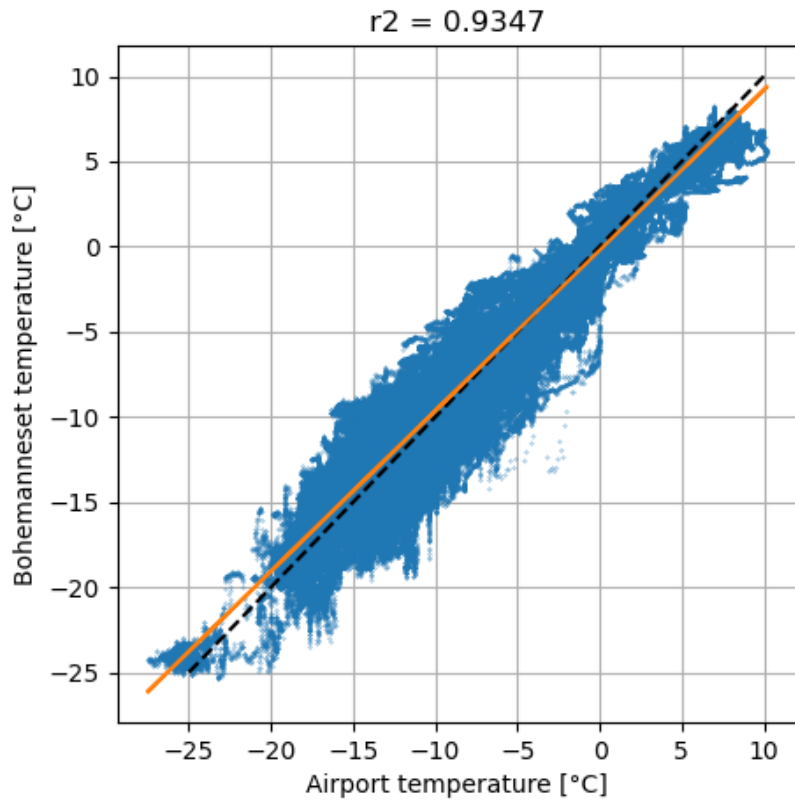
Figure 16: Linear regression between temperature values measured at BHN and LYR between 19 August 2021 and 22 April 2022. The orange line shows the model function $y = 0.942x - 0.217$. The dashed black line shows the 1-1 relation line.

GILL

Gill Instruments Limited

Certificate of Conformance

This is to certify that:

Product: **1957-0500-60-100   MAXIMET GMX500**

|||||||||||||||||||||||||||||||||||||||||||||||||||

Serial Number: **21050002**

||||||||||||||||||||||||||||||||

Has been manufactured within Gill Instruments Limited Quality Management System, approved to the requirements of BS EN ISO 9001.

The instrument has been tested and calibrated with equipment having full traceability to national standards where applicable and meets the requirements of the Operating Manual Specification and Electrical Conformity, both CE and FCC.

This device complies with part 15 of the FCC rules. Operation is subject to the following two conditions:

(1) This device may not cause harmful interference and
(2) This device must accept any interference received, including interference that may cause undesired operation.

The instrument comes with a **24 Month** warranty against defective materials or workmanship from the date of purchase, providing it has not been tampered with and has been returned through an authorised route to Gill Instruments Limited.

Date created: 25 Jan 2021   Signed by: ....

Les Rann
Quality Engineer

Gill Instruments Limited   Tel: +44 (0)1590 613500
Saltmarsh Park   Fax: +44 (0)1590 613501
67 Gosport Street   E-mail: gill@gillinstruments.com
Lymington   Web: gillinstruments.com
Hampshire
SO41 9EG, UK

View our current Anemometer range here

Doc No: 20020519:   Change Note No: 9508   Approved by: Les Rann   Issue: 02   Date released: 26th March 2019

Figure 17:   Calibration Certificate AWS 1872.

Gill Instruments Limited

Certificate of Conformance

This is to certify that:

Product: **1957-0500-60-100   MAXIMET GMX500**

Serial Number: **20510001**

Has been manufactured within Gill Instruments Limited Quality Management System, approved to the requirements of BS EN ISO 9001.

The instrument has been tested and calibrated with equipment having full traceability to national standards where applicable and meets the requirements of the Operating Manual Specification and Electrical Conformity, both CE and FCC.

This device complies with part 15 of the FCC rules. Operation is subject to the following two conditions:

(1) This device may not cause harmful interference and
(2) This device must accept any interference received, including interference that may cause undesired operation.

The instrument comes with a **24 Month** warranty against defective materials or workmanship from the date of purchase, providing it has not been tampered with and has been returned through an authorised route to Gill Instruments Limited.

Date created: 14 Dec 2020   Signed by: ....

Les Rann
Quality Engineer

Gill Instruments Limited
Saltmarsh Park
67 Gosport Street
Lymington
Hampshire
SO41 9EG, UK

Tel: +44 (0)1590 613500
Fax: +44 (0)1590 613501
E-mail: gill@gillinstruments.com
Web: gillinstruments.com

View our current Anemometer range here

Doc No: 20020519:   Change Note No: 9508   Approved by: Les Rann   Issue: 02   Date released: 26th March 2019

Figure 18:   Calibration Certificate AWS 1883.

GILL

Gill Instruments Limited

Certificate of Conformance

This is to certify that:

Product: **1957-0500-60-100   MAXIMET GMX500**

Serial Number: **21360045**

Has been manufactured within Gill Instruments Limited Quality Management System, approved to the requirements of BS EN ISO 9001.

The instrument has been tested and calibrated with equipment having full traceability to national standards where applicable and meets the requirements of the Operating Manual Specification and Electrical Conformity, both CE and FCC.

This device complies with part 15 of the FCC rules. Operation is subject to the following two conditions:

(1) This device may not cause harmful interference and
(2) This device must accept any interference received, including interference that may cause undesired operation.

The instrument comes with a **24 Month** warranty against defective materials or workmanship from the date of purchase, providing it has not been tampered with and has been returned through an authorised route to Gill Instruments Limited.

Date created: 3 Sep 2021   Signed by: ....

Les Rann
Quality Engineer

Gill Instruments Limited   Tel: +44 (0)1590 613500
Saltmarsh Park   Fax: +44 (0)1590 613501
67 Gosport Street   E-mail: gill@gillinstruments.com
Lymington   Web: gillinstruments.com
Hampshire
SO41 9EG, UK

View our current Anemometer range here

Doc No: 20020519:   Change Note No: 9508   Approved by: Les Rann   Issue: 02   Date released: 26th March 2019

Figure 19:   Calibration Certificate AWS 1924.